Research in Astron. Astrophys. **2012** Vol. **12** No. **9**, 1197–1242
http://www.raa-journal.org *http://www.iop.org/journals/raa*

Research in Astronomy and Astrophysics

INVITED REVIEWS

The Large Sky Area Multi-Object Fiber Spectroscopic Telescope (LAMOST)

Xiang-Qun Cui[2], Yong-Heng Zhao[1], Yao-Quan Chu[3], Guo-Ping Li[2], Qi Li[1], Li-Ping Zhang[2], Hong-Jun Su[1], Zheng-Qiu Yao[2], Ya-Nan Wang[2], Xiao-Zheng Xing[3], Xin-Nan Li[2], Yong-Tian Zhu[2], Gang Wang[1], Bo-Zhong Gu[2], A-Li Luo[1], Xin-Qi Xu[2], Zhen-Chao Zhang[2], Gen-Rong Liu[2], Hao-Tong Zhang[1], De-Hua Yang[2], Shu-Yun Cao[1], Hai-Yuan Chen[2], Jian-Jun Chen[1], Kun-Xin Chen[2], Ying Chen[1], Jia-Ru Chu[3], Lei Feng[1], Xue-Fei Gong[2], Yong-Hui Hou[2], Hong-Zhuan Hu[3], Ning-Sheng Hu[2], Zhong-Wen Hu[2], Lei Jia[1], Fang-Hua Jiang[2], Xiang Jiang[2], Zi-Bo Jiang[2], Ge Jin[3], Ai-Hua Li[2], Yan Li[4], Ye-Ping Li[2], Guan-Qun Liu[2], Zhi-Gang Liu[3], Wen-Zhi Lu[2], Yin-Dun Mao[4], Li Men[1], Yong-Jun Qi[2], Zhao-Xiang Qi[4], Huo-Ming Shi[1], Zheng-Hong Tang[4], Qing-Sheng Tao[2], Da-Qi Wang[1], Dan Wang[1], Guo-Min Wang[2], Hai Wang[2], Jia-Ning Wang[2], Jian Wang[3], Jian-Ling Wang[1], Jian-Ping Wang[3], Lei Wang[2], Shu-Qing Wang[1], You Wang[2], Yue-Fei Wang[2], Ling-Zhe Xu[2], Yan Xu[1], Shi-Hai Yang[2], Yong Yu[4], Hui Yuan[1], Xiang-Yan Yuan[2], Chao Zhai[3], Jing Zhang[5], Yan-Xia Zhang[1], Yong Zhang[2], Ming Zhao[4], Fang Zhou[2], Guo-Hua Zhou[2], Jie Zhu[2] and Si-Cheng Zou[1]

[1] National Astronomical Observatories, Chinese Academy of Sciences, Beijing 100012, China; *yzhao@lamost.org*
[2] Nanjing Institute of Astronomical Optics and Technology, National Astronomical Observatories, Chinese Academy of Sciences, Nanjing 210042, China
[3] University of Science and Technology of China, Hefei 230026, China
[4] Shanghai Astronomical Observatory, Chinese Academy of Sciences, Shanghai 200030, China
[5] Institute of Architecture Design and Research, Chinese Academy of Sciences, Beijing 100190, China

Received 2012 July 19; accepted 2012 August 10

Abstract The Large Sky Area Multi-Object Fiber Spectroscopic Telescope (LAMOST, also called the Guo Shou Jing Telescope) is a special reflecting Schmidt telescope. LAMOST's special design allows both a large aperture (effective aperture of 3.6 m–4.9 m) and a wide field of view (FOV) (5°). It has an innovative active reflecting Schmidt configuration which continuously changes the mirror's surface that adjusts during the observation process and combines thin deformable mirror active optics with segmented active optics. Its primary mirror (6.67 m×6.05 m) and active Schmidt mirror (5.74 m×4.40 m) are both segmented, and composed of 37 and 24 hexagonal sub-mirrors respectively. By using a parallel controllable fiber positioning technique, the focal surface of 1.75 m in diameter can accommodate 4000 optical fibers. Also, LAMOST has 16 spectrographs with 32 CCD cameras. LAMOST will be the telescope with the highest rate of spectral acquisition. As a national large scientific project, the LAMOST project was formally proposed in 1996, and approved by the Chinese government in 1997. The construction started in 2001, was completed in 2008 and passed the official acceptance in June 2009. The LAMOST pilot survey was started in October 2011 and the spectroscopic survey will launch in September 2012. Up to now, LAMOST has released more than 480 000 spectra of objects. LAMOST will make an important contribution to the study of the large-scale structure of the Universe, structure and evolution of the Galaxy, and cross-identification of multi-waveband properties in celestial objects.

Key words: techniques: wide field telescope — active optics — multi fiber — spectroscopy survey — data reduction

1 INTRODUCTION

The LAMOST (Large Sky Area Multi-Object Fiber Spectroscopic Telescope) is a special reflecting Schmidt telescope with an effective aperture of 3.6–4.9 m, a focal length of 20 m and a field of view (FOV) of 5° (Wang et al. 1996). It is also called the Guo Shou Jing Telescope. Its focal ratio is 5. Its optical system is designed with three major components, namely Ma, Mb, and a focal surface. The correcting mirror Ma (5.72 m×4.40 m) is made up of 24 hexagonal plane sub-mirrors; the primary mirror Mb (6.67 m×6.05 m) has 37 hexagonal spherical sub-mirrors. In the process of observation, Ma is capable of synchronously changing its specific aspherical figure to give excellent optical quality (Su et al. 1998). The focal surface has 4000 precisely positioned fibers connected to 16 spectrographs with a distributive parallel-controllable fiber positioning system (Xing et al. 1998), thus LAMOST can observe up to 4000 objects simultaneously.

LAMOST adopts an innovative active optics technique, achieved by changing its mirror surface continuously to achieve a series different reflecting Schmidt systems. This novel concept and unique design broke through the bottleneck of former astronomical instruments that could not combine a large clear aperture with a wide FOV. The new active optics system creatively developed in LAMOST is used for correcting Ma, which is a combination of the thin deformable mirror active and segmented active optics. The distributive parallel-controllable fiber positioning technique is also an advanced technology which solved the problem of simultaneously and accurately locating 4000 astronomical objects. LAMOST opened up the ability to have a large scale optical fiber spectroscopic sky survey with as many as 4000 optical fibers.

The Report by the International Review Committee Meeting for the LAMOST project said in 2005: “LAMOST will be a world-class survey instrument that is adaptable to a broad range of important, astrophysical problems. Its potential gain, judged by the product of collecting aperture and number of fibers is a factor of more than 10 to 15 greater than the Sloan Digital Sky Survey (SDSS) or the 2-degree Field survey (2dF). Achieving this high value for the noted figure of merit is an enormous step forward, opening up a wide range of ‘discovery space.’ There is a need for a wide-field, spectroscopic capability to follow up the panoramic imaging surveys being conducted or planned at a variety of wavelengths. LAMOST is therefore well motivated and has a niche that distinguishes it from other projects, which have smaller apertures, smaller fields of view, fewer fibers that feed spectrographs or a combination of these properties.”

LAMOST is the most powerful spectroscopic survey telescope for researches of wide field and large sample astronomy (Chu & Cui 1996). The key scientific goals of LAMOST include: (1) the extragalactic spectroscopic survey of the large scale structure of the Universe and the physics of galaxies; (2) the stellar spectroscopic survey of the structure of the Galaxy; (3) the cross identification of multi-waveband surveys (Zhao 1999). The spectroscopic survey carried out by LAMOST of nearly 10 million galaxies and quasars will make a substantial contribution to the study of extragalactic astrophysics and cosmology, such as the large scale structure of the Universe, baryon acoustic oscillations, dark energy and dark matter, the formation and evolution of galaxies, the accretion process of massive black holes in active galactic nuclei, and so on. Its spectroscopic survey of nearly 10 million stars will make a substantial contribution to the study of stellar astrophysics and the structure of the Galaxy, such as the spheroidal substructure of the Galaxy, the galactic gravitational potential and the distribution of dark matter in the Galaxy, extremely metal poor stars and hypervelocity stars, 3D extinction in the Galaxy, the structure of thin and thick disks of the Galaxy, and so on. Its spectroscopic survey combined with surveys in other wavebands, such as radio, infrared, ultraviolet, X-ray and gamma-ray, will make a substantial contribution to the cross-identification of multi-waveband properties in celestial objects.

The LAMOST project was suggested by a research group headed by Shou-Guan Wang and Ding-Qiang Su, members of the Chinese Academy of Sciences (CAS), and was supported widely by the Chinese astronomical community. After repeated reviews, a formal proposal for the project was listed into the Chinese National Major Science Program in 1996.

The main characteristics of LAMOST were designed as follows:

Spherical Primary Mirror (Mb)	6.67 m×6.05 m
Active Aspherical Correcting Mirror (Ma)	5.72 m×4.4 m
Effective aperture	3.6 m∼4.9 m in diameter
Field of view	5°
Focal length	20 m
Focal ratio	5
Focal surface	1.75 m in diameter
Number of fibers	4000
Spectral coverage	370–900 nm
Spectral resolution power	$R = 1000, 1500$
Observable sky	–10° $\sim +90^\circ$ declination

The LAMOST project was approved as a national major science project by the Chinese government in April 1997. LAMOST started to be constructed in September 2001. The installation of all LAMOST systems was completed on time in August 2008. The telescope is located at the Xinglong station of National Astronomical Observatories, Chinese Academy of Sciences (NAOC).

After the two year commissioning period starting in 2009, a pilot spectroscopic survey was performed using LAMOST from October 2011 to June 2012.

2 TELESCOPE

2.1 Concept and Innovation

The Large Sky Area Multi-object Fiber Spectroscopic Telescope (LAMOST) is an innovative and unique telescope, which is a special reflecting Schmidt telescope specialized for conducting spectroscopic surveys with a wide FOV and a large aperture (Wang et al. 1996).

To achieve the key scientific goals of LAMOST, a clear aperture with diameter of about 4 m for observing deep celestial objects, a 5° FOV that can accommodate 4000 optical fibers for observing 4000 objects simultaneously, and the ability to conduct a fast survey with the goal of cross identification in multi-waveband data were specified. Obviously, a telescope with both a wide field and a large aperture is required.

Before LAMOST, there were some optical systems that strived to achieve a wide FOV and a large aperture. One is the two mirror optical system with a corrector at its primary focus or

Cassegrain focus to enlarge the FOV to $2^\circ \sim 3^\circ$, such as the 2dF survey project (Wynne 1989; Jones 1994), and SDSS project (Gunn & Knapp 1993). The aperture size of this type of wide field system is limited by the transparency of the optical material obtained for the corrector, and also it is difficult to enable a 5° FOV even with the corrector placed at its primary focus. Willstrop proposed a modified Paul-Baker three mirror optical system (Willstrop 1984), using three aspherical reflecting mirrors with diameters of 3, 4 and 5 meters respectively to get a clear aperture of 4-m and a FOV of 5°. One could see that the Willstrop system has a larger area of light blockage, and its rather fast f-ratio is both unfit and inconvenient for multi-object fiber spectroscopic observation. Moreover, the three reflecting aspherical mirrors will cost much more for fabrication, especially for a large aperture, and it is difficult to enlarge the aperture using this design for future extremely large wide field telescopes.

The Schmidt system is a famous wide field optical system invented in 1931 (Schmidt 1931). The key feature of the Schmidt system is a transparent aspherical plate set at the center of curvature of the spherical mirror. Due to the system's symmetry with respect to incoming on-axis and off-axis light beams, such an optical system can deliver very good, distortion-free images over a large FOV. This invention revolutionized the production of deep sky atlases in the photographic era after 1945, such as the famous Palomar sky survey and UKST survey projects. The Schmidt system could certainly obtain a large FOV of 5° and f-ratio of 5 to fit the optical fiber design, but the problem is how to get a large aperture? There are three disadvantages in the Schmidt system: (1) its aperture is limited by the transparent material; (2) the tube is about two times longer than normal telescopes; (3) it has chromatic aberration. Obviously, with these shortcomings, it is difficult to obtain a large aperture with a Schmidt telescope. Until the completion of LAMOST, the largest Schmidt telescope was 1.34 m in Tautenburg Observatory in Germany.

Chinese astronomers started to develop their own versions of the Schmidt telescope in the 1950s. Shi-Jie Yang developed the first Schmidt camera in 1956 (Yang 1957). Ding-Qiang Su published his first research paper on a Schmidt system in 1958 (Su 1958), and then more papers in 1962 and 1988 (Su 1962; Wang & Su 1983; Su 1988). In his paper in 1962, Su was probably one of the earliest researchers to propose the reflecting Schmidt optical system. With a reflecting Schmidt system, the disadvantages in the aperture limitation due to the available refracting optical material and the chromatic aberration can be overcome. In Europe, Lemaitre also studied the Schmidt optical system (Lemaitre 1984, 2009) and obtained the optimized value of length in designing a reflecting Schmidt telescope.

To overcome the disadvantage of a very long tube, and the correspondingly huge telescope mounting and very large enclosure, Shou-Guan Wang proposed the quasi meridian transit configuration for LAMOST (Fig. 1). In this configuration, the optical axis between the aspherical correcting mirror Ma and the spherical primary mirror Mb is fixed and lies in the meridian plane. The aspherical correcting mirror Ma is used not only as the correcting mirror but also as a coelostat tracking the motion of celestial objects during about 1.5 h of observation while they are passing through the meridian. The focal surface is located between Ma and Mb, where 4000 optical fibers are mounted to aim at celestial objects and direct their light to 16 spectrographs. In this configuration, the tube is fixed and the tracking is by Ma rather than by the whole optical system like normal telescopes, so a different aspheric shape of Ma is required for different sky areas and different times during tracking. To achieve this configuration, Ding-Qiang Su proposed applying active optics to obtain a different aspherical shape of Ma during the observation. When observing in a different sky direction and during a different time in the tracking process, Ma has a different aspherical shape and LAMOST becomes a different reflecting Schmidt telescope. In other words, during the process of tracking the celestial objects, while the system is being controlled by the active optics, a series of reflecting Schmidt optical systems is working in sequence to form the large aperture reflecting Schmidt telescope. Traditionally, such an optical system could not be realized. LAMOST is a special reflecting Schmidt system, a new type of wide field telescope with a large aperture. To acknowledge Wang and

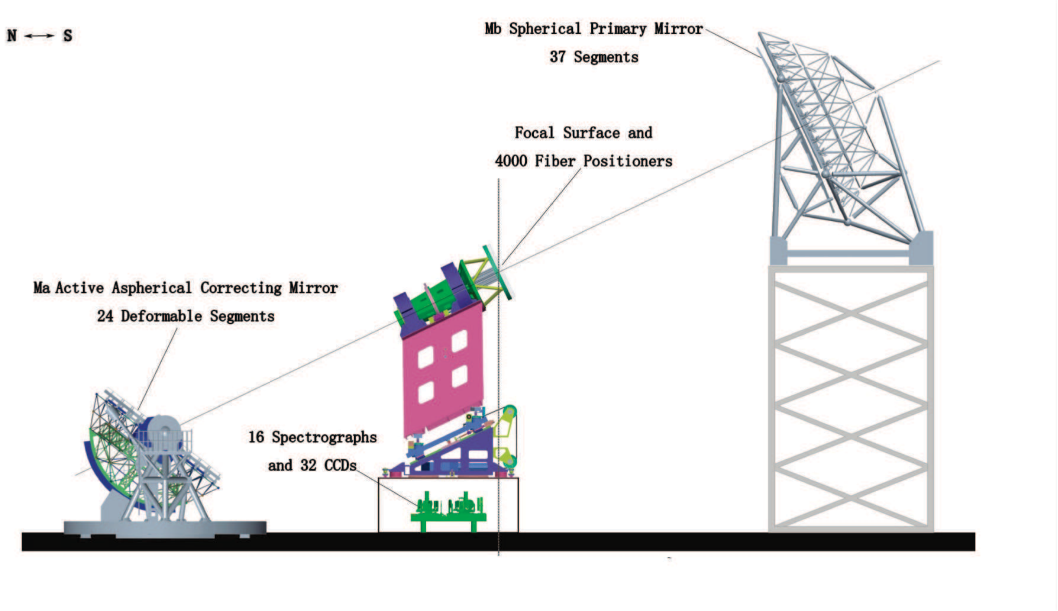

Fig. 1 Configuration of LAMOST.

Su's innovative contribution, we call this new type of telescope the Wang-Su Reflecting Schmidt Telescope (System).

In the early stage of LAMOST, Wang and Su studied and proposed some other configurations for LAMOST in 1992 (Wang & Su 1992) and 1994 (Wang et al. 1994). One thing that should be specially mentioned here is the new idea to apply active optics to get a continuously changing aspherical shape of the mirror for a large telescope like the Arecibo radio telescope by Su in 1986 (Su et al. 1986). Also as in LAMOST, the active optics applied for achieving the required special optical system, by creating the continuously changing aspherical shape of the mirror, is different than the active optics applied in previous telescopes, which are mainly for correcting gravitational and thermal deformation and maintaining the required accurate surface shape of the mirror.

The LAMOST implementation of the Wang-Su Reflecting Schmidt system is a new configuration to obtain both a wide field and a large aperture for a telescope, but also has a simplified structure and the design greatly reduced the cost for the very large telescope, in particular (1) its two large mirrors are only composed of plano and spherical mirrors; (2) it does not have a huge telescope mounting; (3) it does not have a very large telescope enclosure. Another advantage of LAMOST is that the change in altitude angle is very small during the observation, so there is no obvious change in gravitational force exerted on its tracking structure and mirror support system.

To build this innovative telescope, there are some the world class technical challenges that must be resolved, especially (1) the active optics to create and control the continuously varying aspherical shape of the correcting mirror from a plano surface; (2) to reduce the cost, new technologies using active optics are implemented in the two large segmented mirrors, forming one optical system; (3) developing a new method for controlling the optical fiber positioning system with 4000 optical fibers. During the construction of LAMOST, all key technologies have been successfully developed, which not only allowed LAMOST to have the highest rate of data acquisition for an optical fiber spectral telescope, but also advanced Chinese telescope technology to an international level, gaining the ability to build extremely large telescopes such as the 30 m telescope in the near future.

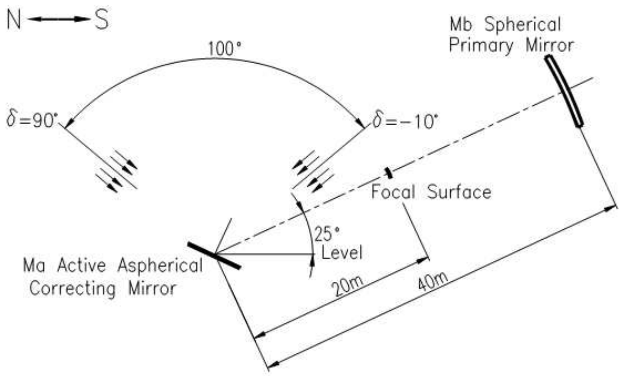

Fig. 2 The optical system of LAMOST.

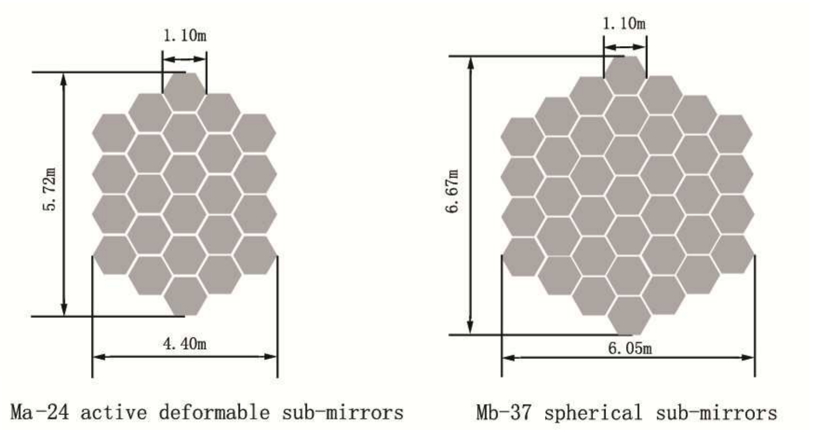

Ma-24 active deformable sub-mirrors

Mb-37 spherical sub-mirrors

Fig. 3 Two segmented mirrors.

2.2 Optical Configuration

LAMOST's configuration is shown in Figure 1. It is aligned in a North-South direction. The optical system of LAMOST consists of the active aspherical correcting mirror Ma, the spherical primary mirror Mb and the focal surface (Fig. 2). They are separately installed on three piers. The primary mirror and the focal surface are fixed to their foundations along the optical axis, which lies in the meridional plane and has a 25° inclination with respect to the horizontal for obtaining a smaller angle of incidence. Ma is located at the center of curvature of Mb on an alt-azimuth mounting. During observation, Ma has to rotate around the altitude and azimuth axes to track objects and reflects starlight to Mb. The celestial objects are observed for 1.5 h on average before and after they pass through the meridian. The sky to be observed covers $10^\circ \leq \delta \leq 90^\circ$. The designed angular diameter of the FOV is 5° for $-10^\circ \leq \delta \leq 60^\circ$ and 3° for $60^\circ \leq \delta \leq 90^\circ$. There are 24 active deformable sub-mirrors for Ma and 37 sub-mirrors for Mb (Fig. 3). All sub-mirrors (segments) are hexagonal and 1.1 m long measured across the diagonal. The thickness is 25 mm for Ma and 75 mm for Mb. The dimension of the segmented primary mirror Mb is 6.67 m $\times$ 6.05 m, and Ma is 5.72 m $\times$ 4.40 m. The radius of curvature of Mb is 40 m. The focal length of the telescope is about 20 m with an f-ratio of 5, which is the best f-ratio for this design of optical fiber spectroscopy.

2.3 Variable Aspheric Surface of Ma

For the case of the reflecting Schmidt system, the aspherical correcting mirror must be tilted and the entrance pupil is on the plane perpendicular to the optical axis as shown in Figure 4. The x'-axis is along the optical axis of the system, and the y'-axis is vertical and in the plane of the entrance pupil. The z'-axis is perpendicular to the plane x'–y'. If the correcting mirror is at the position of the entrance pupil and perpendicular to the optical axis, the aspherical shape of the correcting mirror is approximately expressed as Equation (1) according to the formula for the refracting Schmidt corrector with an index of refraction $n = -1$.

$$t' = -\frac{y'^4 - 2kr^2y'^2}{64f^3} \, . \tag{1}$$

The above equation can be written in the following form if any point on the correcting mirror is expressed by dimensions of coordinates y' and z'.

$$t' = -\frac{(y'^2 + z'^2)^2 - 2kr^2(y'^2 + z'^2)}{64f^3} \, . \tag{2}$$

Using coordinates y and z to express Equation (2) according to the relationship of the two coordinate systems shown in Figure 4, and also considering the change in optical path due to the tilted mirror, it becomes

$$t = -\frac{(y^2\cos^2\theta + z^2)^2 - 2kr^2(y^2\cos^2\theta + z^2)}{64f^3\cos\theta} \, , \tag{3}$$

where t, y and z are the coordinates of the point on the correcting mirror, so Equation (3) expresses the aspherical shape of the correcting mirror. r is the radius of the entrance pupil, f is the focal distance of the primary mirror, θ is the angle between the normal of the vertex of the correcting mirror and the optical axis, and k is a constant and is called the neutral zone height in the optical design. Generally speaking, the constant k corresponds to the position of the focus for which the spherical aberration is eliminated. When different values of k are selected, the position of the optimal focus changes, and the aspherical shape of the mirror also changes. The important thing that should be noticed is for any k, the image quality at the center of the FOV is always good if the focus is put at the optimal position, but images at the edge and other parts of the FOV are different, that is to say the off axis aberration is different. To obtain the least off axis aberration, k should equal 1.5. This pioneering work was done by Gerard Lemaitre in his study on the reflecting Schmidt system (Lemaitre 1984). He found that if $k = 1.5$, one can get good image quality in the whole field of view. Once k is selected, the aspherical shape is uniquely defined. Equation (3) is approximated by the third-order spherical aberration since higher-order terms are negligible. This expression is already accurate enough for this system with f/5. One can express it by adding higher order terms, in which case the shape of the aspherical surface of the correcting mirror will become more accurate.

In LAMOST, the aspheric shape of Ma is expressed by Equation (3) (Wang et al. 1996). The k is taken as 1.5 for LAMOST to get the best image quality for the whole field of view. The angle θ varies between 7.3° and 57.3° as the field to be observed varies between $-10^\circ \le \delta \le 90^\circ$ on the meridian. The y-axis rotates around the normal of the vertex of Ma (θ also changes slightly) during 1.5 h of tracking. Thus the depth t of any point on Ma is not constant. This means that in such a Schmidt system the shape of the correcting mirror must be changed with each different δ during the tracking process. The maximum required deviation of sub-mirrors from the closest plane is only about 9.1 μm for 1.5 h of tracking. This is realized by thin deformable mirror active optics. The center of curvature of Mb is located in the optical system, which is very convenient for using a wavefront monitor to measure the co-centers of all the segments in Mb.

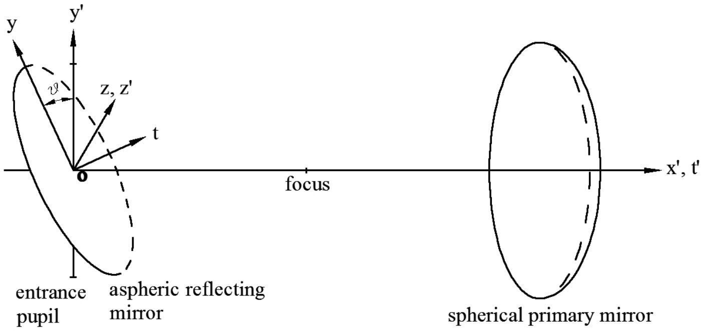

Fig. 4 Coordinate system of the reflecting Schmidt system.

2.4 Simulation of the Observing Process and Image Quality

As mentioned in Section 2.1, the optical system of LAMOST is a special optical system. During the process of tracking the celestial objects, the Schmidt system is continuously changing because the aspherical shape of Ma also changes. How the image can be obtained by superimposing those images acquired with varying configurations of the reflecting Schmidt telescope is a problem that needs to be understood. Therefore, computer simulations of the observing process have been done. These include pointing and tracking of Ma, guiding the position and direction of a star in the FOV, rotation of the FOV and the effect of atmospheric refraction. Finally, images are formed by a series of images obtained over time that are superposed together. In this simulation, the entrance pupil is taken as a circle with a diameter of 4 m and positioned at the center of Mb. The constant k is taken as 1.5. Focal distance is 20 m. The angle of incidence θ is found according to the declination δ and hour angle t, where the star is observed. The tracking time is 1.5 h while the star is passing through the meridian. Results are given in Table 1 and Figure 5. The image quality is given by a circle with diameter in which 80% of the light energy is concentrated. The unit is arcsec.

Table 1 shows the imaging quality for three situations: (1) the object at the center of FOV in the meridian plane, (2) tracking for 1.5 h without the effects of the atmosphere, (3) tracking for 1.5 h with the effects of the atmosphere. The corresponding diameters of the FOV are $0°$, $3°$ and $5°$, and columns (a), (b) and (c) correspond to cases (1), (2) and (3) respectively.

Figure 5 gives the spot diagrams for four sky areas. Spots in column (a) correspond to the case where the objects are at the center of the FOV in the meridional plane. Spots in column (b) show the star images after tracking for 1.5 h, and spots in column (c) are the star images after tracking for 1.5 h and including the effect of atmospheric refraction. Large circles in Figure 5 correspond to the maximum FOV, which are $5°$ for $\delta = -10°$, $40°$ and δ=60° and $3°$ for δ=90°. The small circles show the positions of half the FOV.

According to Equation (3) it is obvious that the image quality of LAMOST is related to the incident angle θ. The worst case is having a large incident angle in the sky area close to the North Pole $60° \leq \delta \leq 90°$. Since the sky area is small there, it is reasonable to use an FOV of $3°$. The range of large sky area near the equator is the most interesting for astronomical observation and has a small angle of incidence. From the result of the image quality in Table 1 and Figure 5, one can see that most of the sky areas used for observing have an image quality better than $1''$.

2.5 Focal Surface and Rotation of the Field of View

The optimal focal surface of a Schmidt system is an aspheric surface, but usually it is approximated as a sphere with its radius of curvature at about the focal distance. However, LAMOST is different

Table 1 Image Quality with 80% of the Light Entering the Diameter Expressed in arcsec

2W	0°			3°			5°		
δ	a	b	c	a	b	c	a	b	c
–10°	0.029	0.029	0.029	0.158	0.150	0.853	0.250	0.259	1.463
0°	0.029	0.029	0.029	0.247	0.236	0.525	0.390	0.408	0.899
10°	0.029	0.029	0.029	0.342	0.321	0.410	0.534	0.556	0.686
20°	0.029	0.029	0.029	0.446	0.415	0.439	0.689	1.711	0.754
30°	0.029	0.029	0.029	0.561	0.516	0.524	0.861	1.879	0.901
40°	0.029	0.029	0.029	0.692	0.626	0.624	1.055	1.068	1.073
50°	0.029	0.029	0.029	0.843	0.750	0.761	1.280	1.280	1.311
60°	0.029	0.029	0.029	1.024	0.894	0.934	1.548	1.529	1.590
70°	0.029	0.029	0.029	1.044	1.065	1.127			
80°	0.029	0.029	0.029	1.263	1.272	1.376			
90°	0.029	0.029	0.029	1.552	1.546	1.724			

due to the optical system not having rotational symmetry. It is found that even though the optimal focal surface of the reflecting Schmidt system is an unsymmetrical aspheric surface, it can be regarded as a sphere with its radius of curvature being about the focal distance, but the axis of the focal surface is slightly tilted relative to the optical axis of the spherical primary. The angle between axes can be expressed as in Equation (4)

$$\alpha = -0.01250463 - 0.030305557\delta - 0.006611554\delta^2 + 0.003138813\delta^3 - 0.004454463\delta^4 , \qquad (4)$$

where α is the angle in degrees between axes of the focal surface and the primary mirror, and δ is the declination of the object at the center of the field in radians. The maximum α is about 5.4 arcmin.

Like all telescopes with an alt-azimuth mounting, LAMOST has field rotation because of the mounting of Ma. When the hour angle goes from $-0.75^{\rm h}$ to $0.75^{\rm h}$, the rotation angle goes from $3.3827°$ to $-3.3827°$ for $\delta = -10°$ and from $-11.25°$ to $11.25°$ for δ= $90°$. It shows that the sign of the angle changes, which means that there must be a position of δ where the field does not rotate. Further study shows that this is at δ=$24.6°$. Over the whole observed sky area, the rotation speed is very smooth (Su & Wang 1997b).

2.6 Effective Aperture and Vignetting

The entrance pupil of LAMOST is the projection of Ma on the direction perpendicular to the optical axis. Ma consists of 24 active sub-mirrors with a total size of 5.72 m×4.40 m. The size of its projection on the direction perpendicular to the optical axis is different when the telescope points to a different area of the sky during the course of tracking. Therefore, the area of the entrance pupil or clear aperture of LAMOST is not fixed and the f-ratio is also not fixed. The effective area of the pupil is calculated and listed in Table 2 for the different sky areas (in δ). In the table, ϕ is used to express the diameter of the circle which has an area equal to the effective area of the pupil. The diameters ϕ for 11 sky areas are given in Table 2, where ϕ_0 and $\phi_{0.75}$ correspond to stars on the meridian and with an hour angle of $0.75^{\rm h}$ respectively.

When the object is not at the center of the FOV, some of the light reflected from the Ma may be reflected outside the area of Mb due to Mb is not being large enough, which causes vignetting in LAMOST.

Figure 6 is a map for stars at δ= –10°, 40° and 90° passing through the meridian. One can notice that the vignetting is different for different areas of the sky, different FOVs and different positions in a same field angle. The vignetting in LAMOST shows axial symmetry when the star is at the center of the FOV and passes through the meridian.

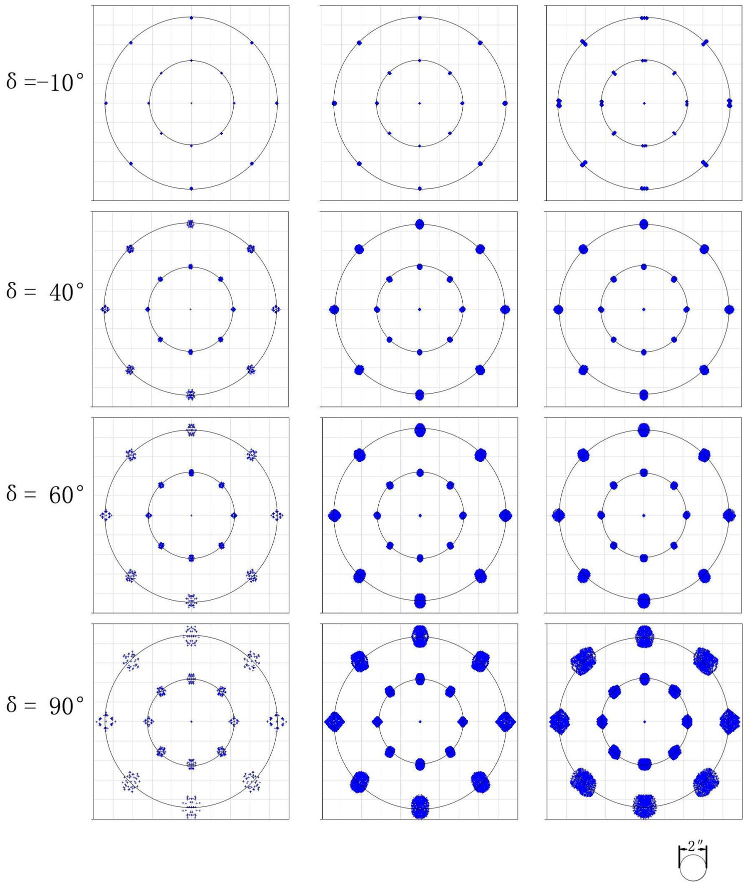

Fig. 5 Spot diagrams for the four sky areas.

Table 2 Clear Apertures for Different δ

δ	–10°	0°	10°	20°	30°	40°	50°	60°	70°	80°	90°
ϕ_0	4881	4844	4788	4714	4620	4506	4371	4215	4036	3832	3602
$\phi_{0.75}$	4870	4833	4777	4702	4608	4495	4361	4206	4029	3828	3602

The coefficient of vignetting is defined as

$$K = \frac{SA - S1}{SA}, \tag{5}$$

where $S1$ is the projected area of the light beam on Mb, and SA is the projected area of the full light beam on Ma for off-axis incident light.

Table 3 gives the vignetting value for $\delta = -10^\circ - 90^\circ$. The FOV angle is $\pm 2.5^\circ$ for $-10^\circ \leq \delta \leq 60^\circ$ and $\pm 1.5^\circ$ for $60^\circ \leq \delta \leq 90^\circ$. The diameter of the focal surface is 1790 mm. In a reference paper, authors made detailed calculations about vignetting but their definition of vignetting is different from that usually used in optics (Xue & Shi 2008).

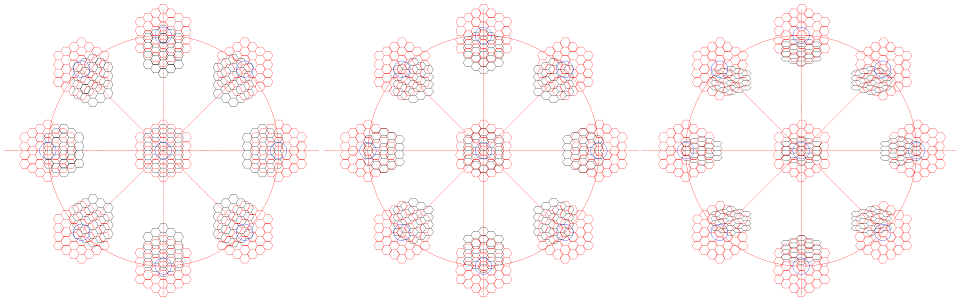

Fig. 6 Vignetting in different areas of the sky (*left-to-right*, $\delta = -10^\circ$, 40° and 90°).

Table 3 Vignetting in LAMOST

δ	sagittal direction	tangent direction	45° direction
–10°	0.2508	0.2790	0.2606
0°	0.2452	0.2756	0.2551
10°	0.2356	0.2703	0.2506
20°	0.2245	0.2629	0.2423
30°	0.2091	0.2530	0.2375
40°	0.2028	0.2401	0.2312
50°	0.1868	0.2235	0.2073
60°	0.1890	0.2025	0.1965
70°	0.0470	0.0014	0.0087
80°	0.0477	0.0000	0.0035
90°	0.0496	0.0000	0.0042

The variable aperture during observation causes the area of the collected light beam to change, and vignetting causes the brightness to be uneven on the focal surface, but these are not major effects for multi-object fiber spectroscopic observations with some correction, which can be performed during the data processing. Considering these, and also the transmission (including the aiming accuracy at celestial objects) not being uniform for all optical fibers, LAMOST is not suitable for diffraction-limited high resolution observations, which means an optical fiber spectroscopic telescope is not suitable for photometry.

2.7 Tracking Times for Different Areas of the Sky

The image quality is related to the angle between the normal of Ma and the optical axis of Mb (which equals the incident angle). When the area observed is moved from $\delta = -10^\circ$ to 90°, the angle is increases from 7.3° to 57.3° and the image quality becomes worse. This means that the image quality is the best at $\delta = -10^\circ$ and the worst at $\delta = 90^\circ$. The image quality is also affected by atmospheric refraction. This effect becomes more severe when the zenith distance is large at $\delta = -10^\circ$. In addition, f-ratio also affects the image quality. The projection of Ma on the direction perpendicular to the optical axis is the largest at $\delta = -10^\circ$ and the least at $\delta = 90^\circ$, so the f-ratio is the fastest at $\delta = -10^\circ$ and the slowest at $\delta = 90^\circ$. Considering all these various factors, when observing an area around the zenith, the image is best. Thus, for a certain image quality, the tracking time may be much longer than 1.5 h in this sky area.

Figure 7 gives the relation between tracking time and image quality. The image quality is expressed in terms of a quantity called E80%, which is given by the diameter of the circle in which 80% of the energy is included, where the x-coordinate is tracking time in hours and the y-coordinate

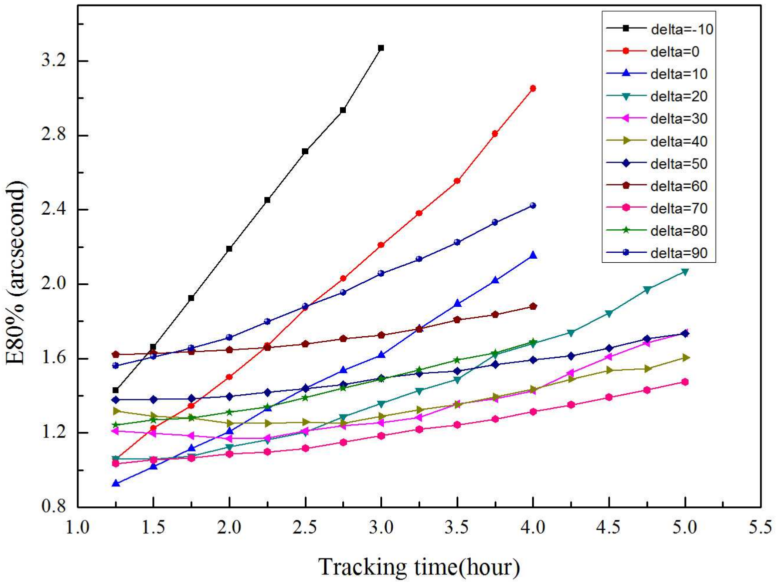

Fig. 7 Relation between tracking time and the quantity E80%.

is image quality in terms of E80% in arcsec. Even Figure 7 shows that the tracking time could be 5 h or more (including tracking before and after the meridian) for the sky area $\delta = 20^\circ \sim 50^\circ$ and 70° if the required resolution of the image (in terms of E80%) should be better than $2''$, but the large hour angle may limited by the working range of the displacement actuators on the active support system of Ma and other limitations. Thus it is better if the observing time is not longer than 4 h, except for special cases.

2.8 Atmospheric Refraction Effects

Atmospherical refraction changes the zenith distance of a celestial body. The change in zenith distance causes the displacement and dispersion of star images. The effects of atmospherical refraction on the star image of LAMOST have been studied, with the result showing that the maximum displacement of star images is $0.859''$ during 1.5 h of observation (Su & Wang 1997a). It means that the maximum deviation of the image from the center of the fiber is $0.859''$. The average deviation is $0.430''$ which equals the positioning error. Comparing this value with the $3.3''$ diameter of the fiber shows it is relatively small, and the loss of light due to the image deviation is also small. In addition, such image deviation will only happen at the largest FOV, when observing the sky area at $\delta = -10^\circ$. As a compromise, the image deviation may not be corrected. The correction could be done by optical fiber positioners when required.

When the zenith distance is not very large, its change caused by atmospherical refraction can be calculated using the approximate formula

$$\rho = z' - z \approx 206265(n-1)\tan z\,, \tag{6}$$

where ρ is the change of zenith distance, z and z' are the real and changed zenith distances respectively, and n is the index of refraction. Applying this formula for different wavelengths, the dispersion can be calculated. For LAMOST, in the waveband $\lambda = 380 \sim 1000\,$nm the maximum dispersion is $2.29''$ which only happens in the area of $\delta = -10^\circ$ (Liu & Yuan 2005). When the celestial body is near the zenith, the dispersion is less than $0.3''$. Considering that the seeing in Xinglong is about $2''$, the dispersion may not be correctable either. If LAMOST could be placed at a site with good seeing, the dispersion should be corrected. Several kinds of atmospherical dispersion correctors have been studied (Liu & Yuan 2005; Su et al. 2012).

2.9 Effect of Segmented Mirrors on the Distribution of Diffraction Energy

In LAMOST, both of the two large mirrors, Ma and Mb, are segmented. The amount and arrangement of sub-mirrors in Ma and Mb are different. The difference in the sizes of the two mirrors causes diffraction in many smaller subareas, which enlarges the point spread function (PSF). At a good astronomical site, atmospheric seeing only allows a telescope with an aperture of less than 30 cm to obtain a diffraction-limited image if adaptive optics is not used. Because adaptive optics cannot be used for a telescope with a large FOV, in this case, for a segmented mirror telescope, a subarea with a diameter of 50$\sim$60 cm is enough. In the case of LAMOST, there is an angle of incidence between the normal of Ma and the optical axis, and the angle of incidence is different for different sky areas and different times during tracking. In all these situations, the superposition of the projection of Ma and Mb is different and the shapes of the subareas divided by the edges of the hexagonal sub-mirrors are complex. Generally speaking, each hexagonal sub-mirror of Ma is divided into three or four subareas. If Ma is approximately perpendicular to the optical axis and there are four subareas, the average surface area of the subareas equals a circular area with a diameter of 0.5 m. As a rough estimate, the distribution of diffracted energy in LAMOST is like a circular hole with a diameter of 0.5 m. This means 84 percent of the light energy is spread over an area of about $0.5''$ (Airy disk). In the case of sky area observed at $\delta = 90°$, the height of the projection of Ma sub-mirrors will be reduced to about half but the width will not change. In this case, 84 percent of the light energy is spread over an area of about $0.5''$ width and $0.75''$ length (Su et al. 2012). Wenli Xu calculated the distribution of the diffraction of energy for LAMOST in detail for four special situations and arrived at a similar conclusion that 80% of the diffracted energy is concentrated within a circle with a diameter of about $0.5''$ for all conditions (Xu et al. 1997). Moreover the atmospheric seeing in Xinglong is about $2''$ on average, and the diameter of the fibers is $3.3''$. Thus, the effect of an enlarged PSF in LAMOST caused by two segmented mirrors is minor and acceptable.

2.10 Stray Light

The enclosure of LAMOST is divided into two parts. One part is a dome for Ma, which is in an open mode during the observation. The other part is a cylindrical tube that encloses the focus and Mb, which is along the optical axis and is about 25.5 m long. During the observation, not only can light from the celestial objects enter the optical system of the telescope, but stray light can also enter from different directions, such as light from the sky background, light from the moon and stars reflected by the ground, light from the outer wall and inner wall of the dome, and some scattered lights directly from Ma into Mb. These lights are not involved with imaging, and scatter multiple times on the inside surface of the cylindrical enclosure, eventually becoming stray light on the focal surface, which interferes with imaging quality as noise.

To avoid the light not involved with imaging from coming into the field of view, or at least reduce the influence of the stray light, three light stops have been set up between the focus and Mb in the cylindrical enclosure along the optical axis, with distances of 15.6, 25.5 and 34.6 meters from the Ma respectively. In LAMOST, when the telescope points at different sky areas, the beam height is different and the vignetting is also different. For example, while the telescope points at a target with low declination, it has a larger beam height and large vignetting, but at high declination there is a smaller beam height and smaller vignetting. The width and height of all three light stops were designed with the goal that there would not be more blockage added into the optical system while trying to keep the vignetting situation unchanged. By setting up three light stops, most light not involved with imaging is effectively blocked.

Although the above implementation of three light stops partly blocks the light not involved with imaging, for those stray lights coming from multiple reflections in the inside of the enclosure, improving the absorption of the coated surface inside the enclosure is important, especially those stray lights around Ma which are just scattered one time before reaching Mb. By using special software to do the calculation and analysis, if the surface absorption could be increased from 90% to 99%, one could reduce the point source light transmittance (θ), which is the characterization of the optical system's level of stray light, one order of magnitude. The work to eliminate stray light in LAMOST is continuing, and further modifications will soon be implemented.

2.11 Active Optics

The field of active optics developed in the 1980s and successfully allowed the aperture of large telescopes to be enlarged from 5 or 6 meters to 8 or 10 meters (Wilson et al. 1987; Noethe et al. 1988; Mast & Nelson 1982). Nowadays, a consensus is that active optics is a key technology for building large telescopes and telescopes with high imaging quality. Active optics are mainly used to correct gravitational deformation and thermal distortion in telescope mirrors and structures, especially to maintain a highly accurate surface shape in the primary mirror of the telescope and the collimation of the optical system, which is impossible with traditional passive optics.

LAMOST represents the first time active optics has been applied for creating a series of aspherical surface shapes in the mirror during the observation, to configure a special optical system which could not be obtained by the design of a traditional optical system. This makes such a new type of telescope possible that uses the Wang-Su reflecting Schmidt design with both a large aperture and wide FOV. The proposal put forward was based on the preliminary study of Su et al. (1986) for a new telescope and development of related technology (Su et al. 1994, 2000).

The implementation of active optics represents the most challenging and crucial part in the LAMOST project. To realize the new concept and reduce the cost for the project, some new technologies in active optics have been developed and new applications created (Su et al. 1998; Su & Cui 1999, 2004; Cui et al. 2004; Zhang & Cui 2005; Zhang 2008):

(1) The active optics system in LAMOST has both segmented mirror active optics and thin deformable mirror active optics in one mirror (Ma), where the active optics simultaneously controls each aspherical surface shape of the 24 hexagonal sub-mirrors in Ma during observations.
(2) The thin deformable mirror active optics of Ma is not only used to correct the gravity and thermal deformation of the structures and the mirrors, as well as the manufacturing and alignment errors, but is also mainly used to create the required aspherical surface shapes of the 24 hexagonal sub-mirrors in real time, where each sub-mirror has an off-axis aspherical shape.
(3) Both the reflecting Schmidt corrector Ma and the spherical primary mirror Mb are segmented with 24 and 37 hexagonal sub-mirrors respectively. LAMOST is the first telescope to use two large segmented mirrors in one optical system.
(4) It is the first project to use non-round deformable mirrors.
(5) Except for being applied in the experimental system (Su et al. 1994), LAMOST is the first case to apply the damping least square method in resolving the active force calculation in real time during observation, a method which is normally only used in the optimization of the optical system design.
(6) A new algorithm and calibration method have been created to resolve the active force displacements simultaneously and accurately, where the sub-mirrors are both thin and non-round.
(7) This is the first time to apply two wavefront sensors in one optical system. One is used to ensure the co-centering of the spherical primary mirror Mb, and the other is to ensure the image quality

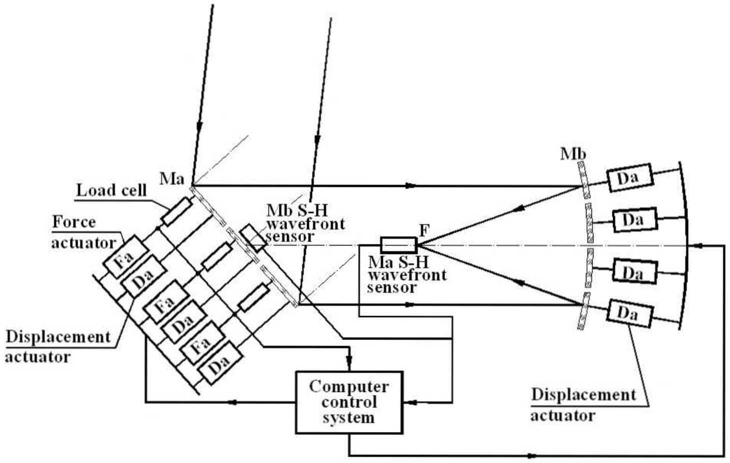

Fig. 8 The schematic of the active optical system in LAMOST.

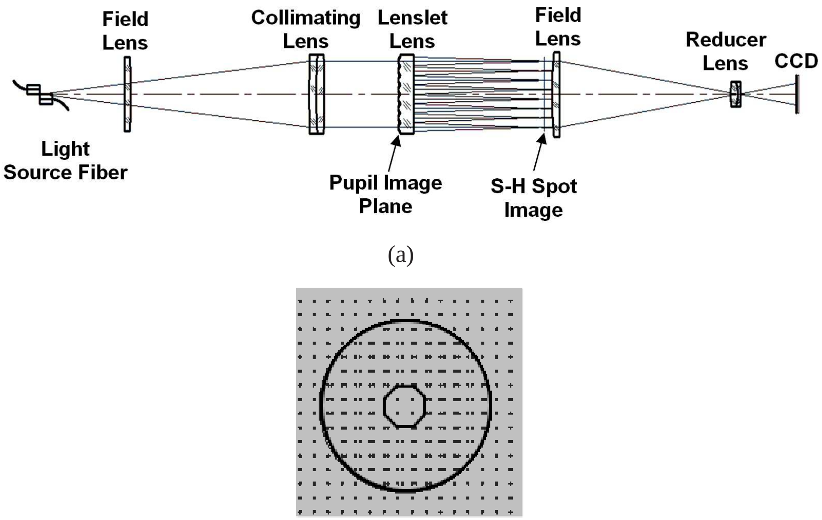

(a)

(b)

Fig. 9 (a) Schematic of the S-H wavefront sensor, (b) the image on its focal plane.

of the whole optical system, especially the continuously changing aspherical surface shape of the active correcting mirror Ma.

(8) Wavefront sensing is performed on the shape and size of the variable pupil.

(9) A closed loop control system is combined with with an open loop control system.

As shown in Figure 8, the active optics system in LAMOST consists of two wavefront sensors, six computers for wavefront analysis, control of the mirror shape and co-focusing (or co-centering) of the sub-mirrors, 200 intelligent controllers (computers), 816 force actuators with load cells, 183 displacement actuators, and 290 displacement sensors.

The schematic of the Shack-Hartmann (S-H) wavefront sensor is shown in Figure 9. The optical system of the S-H wavefront sensor for Ma is shown in Figure 10 as an example, which is located at the center of the focal surface. The wavefront error can be detected by analysis of the difference

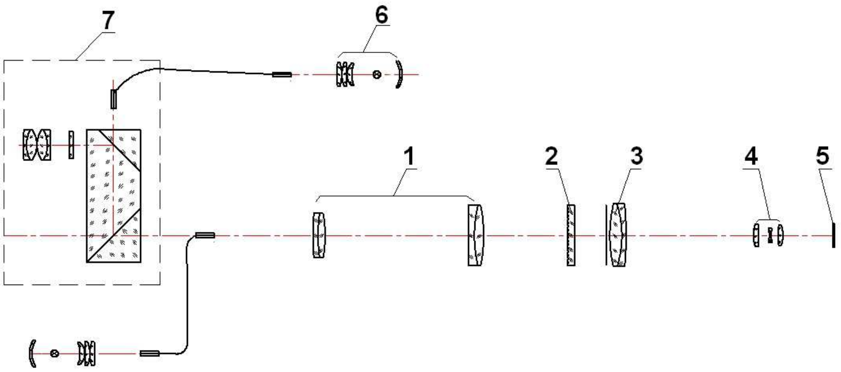

Fig. 10 The optical system of the S-H wavefront sensor used for Ma. 1. Collimating Lens; 2. Lenslet Array; 3. Field Lens; 4. Reducer Lens; 5. CCD; 6. Light Source and Condenser Lens; 7. Used for Checking the Light Path.

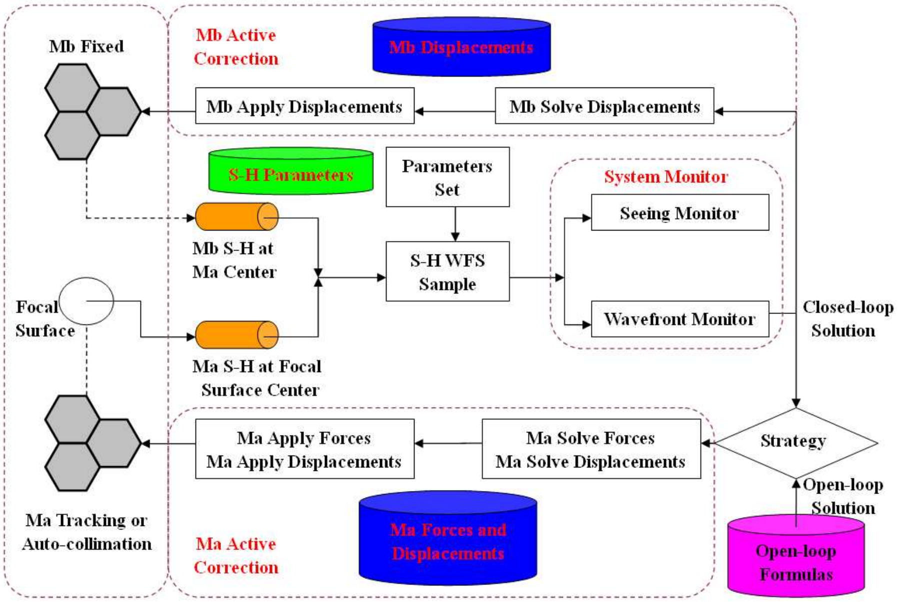

Fig. 11 The block diagram of the wavefront analysis and control.

between the standard image spots (ideal wavefront) and image spots from the deformed wavefront. LAMOST is designed with an accuracy in wavefront measurements of 0.15″.

The process of wavefront analysis uses the deviation from a normal line to specifically analyze the wavefront slope error or the normal line deviation of the wavefront, and to calculate the forces needed in displacement actuators that should be used to correct the mirror shape and the co-focus (or co-centering) of the segmented mirrors. Figure 11 shows the block diagram of the wavefront detection and analysis software of Ma and Mb.

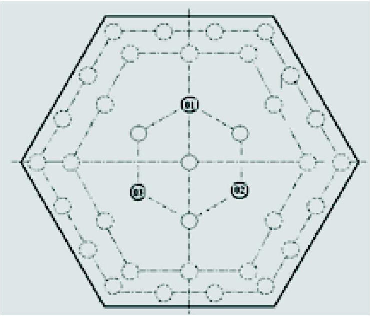

Fig. 12 Distribution of active supports for an Ma-submirror.

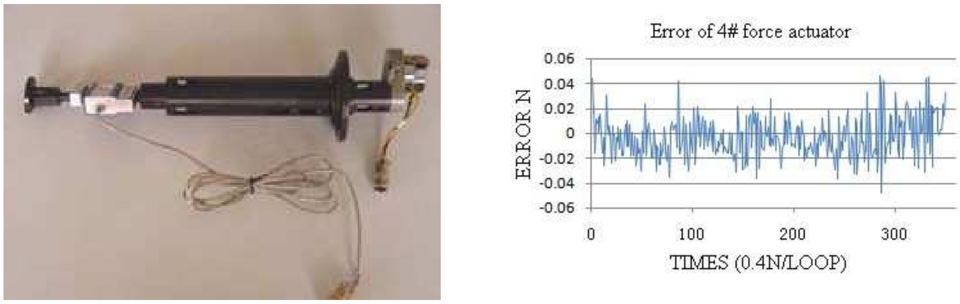

(a) (b)

Fig. 13 (a) Force actuator; (b) a force actuator with sustained accuracy RMS=17.75 mN, $P - V = 46.7$ mN after 15 000 h of test operation.

(a) (b)

Fig. 14 Ma sub-mirrors. (a) after being installed; (b) sub-mirrors after polishing.

There are 120 intelligent controllers that need to get information from 816 load cells and control 816 force actuators, and 12 controllers to control 72 displacement actuators in the Ma active support system, which form the local closed loop control system of LAMOST's active optics. 34 active supports (force actuators) with fixed supports (corresponding to displacement actuators), together with lateral supports for each sub-mirror, compose its complete mirror support system. Figure 12 shows the distribution of the active supports and fixed supports in one Ma sub-mirror.

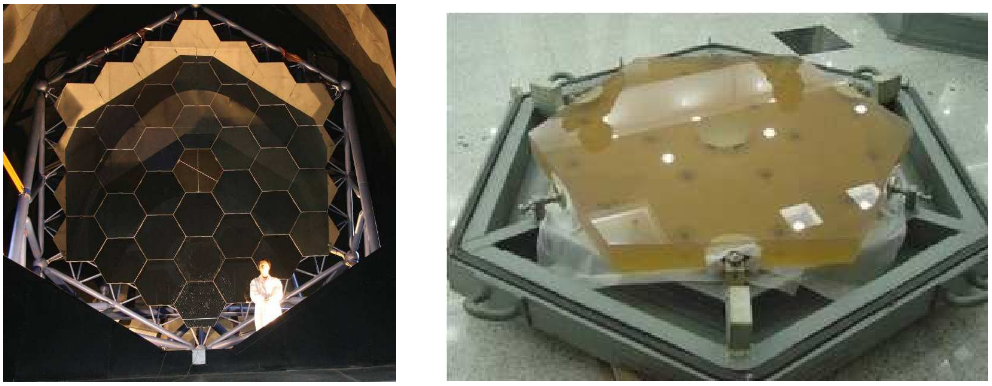

(a) (b)

Fig. 15 Mb. (a) completing the installation of 37 sub-mirrors; (b) a sub-mirror after polishing.

To meet the requirements for LAMOST's tracking speed and image quality, the force actuators are controlled with a minimum time interval of 1.5 min and an accuracy of 50 mN in the force range of [–150N,+150N]. The test results for all 816 force actuators have shown that they are all better than the requirements. Figure 13 shows one test result of a force actuator. All displacement actuators and sensors equipped in Ma and Mb have an accuracy of 30 nm and a dynamic adjustable range of 1 mm.

The S-H wavefront sensor of Mb is mounted at the center of curvature of the spherical primary mirror Mb, that is, the center of Ma. There are 111 displacement actuators for 37 sub-mirrors. The active optics of Mb is only used for maintaining the co-center of 37 sub-mirrors. Because the main source of error is thermal deformations in the structure, the wavefront sensing and frequency of mechanical corrections in the apparatus can be very low, such as once per hour. When displacement sensors are used to maintain the co-center, the S-H wavefront sensor could only do the calibration once per night.

2.12 Optical Performance

The image quality of the telescope normally depends on (1) image quality designed for the optical system; (2) surface shape accuracy of all optical components determined by manufacturing; (3) maintaining an accurate shape of the mirrors in real time by the support system; (4) collimation of the optical system. When the active optics system is being applied, the above requirements, except (1) and the high space frequency error of (2) could be relaxed, and get higher image quality compared with the traditional passive optical system.

In LAMOST, 24 sub-mirrors composing Ma are shown in Figure 14(a). Each sub-mirror has a plano surface, with length 1.1 m corner to corner, and thickness 25 mm (Fig. 14(b)). After completion of the manufacturing, the acceptance test results show that the surface accuracy in terms of RMS of all 30 Ma sub-mirrors, including spares, is between RMS 8.1 nm and 18.9 nm, and is 12.25 nm on average, showing that the diffraction limit is reached.

The complete set of 37 sub-mirrors of Mb is shown in Figure 15(a), with a spherical surface, 1.1m diagonal, and 75 mm thickness for each sub-mirror (Fig. 15(b)). The results from the acceptance test show that the average accuracy of all 40 sub-mirrors, including spares, is 11.2 nm RMS, and the consistency of all sub-mirrors for the 40 m radius of curvature is less than 1.5 mm.

Fig. 16 Ma support structure being installed.

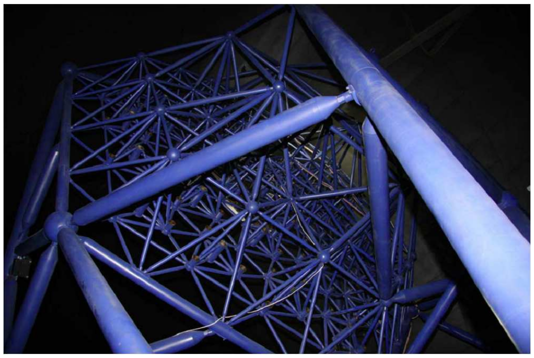

Fig. 17 Support structure.

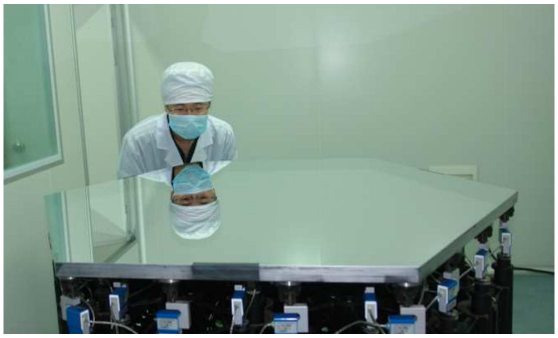

Fig. 18 Ma sub-mirror assembly being tested.

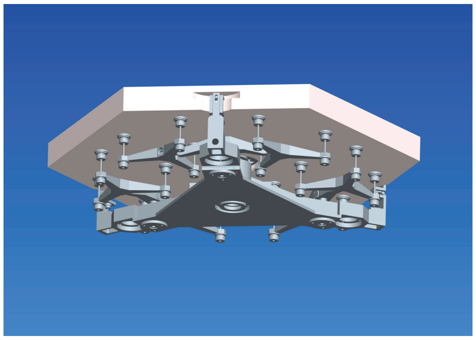

Fig. 19 Mb sub-mirror with its support system (computer model).

All 24 sub-mirrors of Ma are supported by a mirror cell with a truss structure (Cui & Yang 1998; Yang et al. 2005) (Fig. 16), which has an accuracy of 0.312 mm RMS for supporting Ma on the top layer. Figure 18 shows a completed Ma sub-mirror assembly. For Mb, there is also a truss structure to support all 37 sub-mirrors supported on it (Fig. 17). Each sub-mirror of Mb has a very compact whiffletree support system in the axial direction with 18 supports (Fig. 19) and a center support for the lateral direction (Gong et al. 2004). Three displacement actuators on each sub-mirror can control and maintain the position of each sub-mirror in three dimensions accurately for co-centering visible wavelength observations of LAMOST. Also there is a possibility to implement co-phasing for near infrared observations if it is required in the future.

The support system of each sub-mirror should maintain the surface accuracy to very good quality in operation mode. The test results with an interferometer for all sub-mirrors of Ma and Mb with their support systems show that all 24 Ma and 37 Mb sub-mirrors are maintained by their support systems with an average surface error RMS of 21.7 nm and 16.6 nm respectively.

As described in Section 2.1, a Schmidt optical system is composed of a spherical primary mirror and a correcting mirror located at the center of curvature for the spherical primary. For LAMOST, when the surface shape of the correcting mirror Ma is defined by the active optics with $k = 1.5$, the image quality is acceptable at the center of the FOV while it is being controlled by an S-H wavefront sensor; one only needs to make sure the surface shape of the primary mirror is always correct by

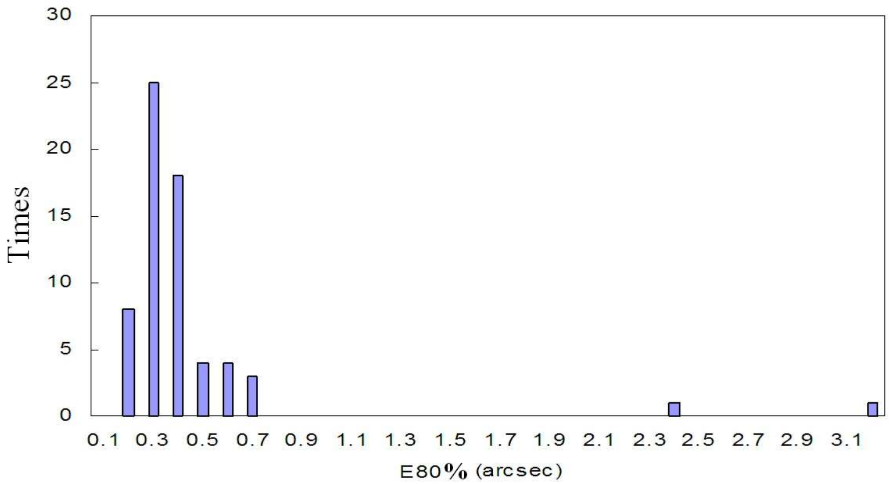

Fig. 20 The statistics of image quality from tracking a 7.2 magnitude star for 132 min (ordinate is the number of times).

using the S-H wavefront sensor located at the center of curvature of the Mb. Thus the off axis image quality in the whole FOV is correct and it performs well as a Schmidt telescope.

The following are some typical test results during commissioning:

Test results with the Shack-Hartmann wavefront sensors Figure 20 shows one of the image quality results of the telescope's optical system during the closed loop control by the active optics, which was tested on 2008 Nov. 21 by the S-H wavefront sensor for Ma while tracking an object at declination 24.25° and hour angle 2.22° for 132 min (Cui et al. 2010). From this test, one can see that during good weather in the Xinglong Station, with seeing conditions about FWHM $3.0''$, as given by the guiding camera's long exposure images, the telescope's optical system had the best image quality of $0.25''$ in terms of E80% (corresponding to an estimated FWHM of $0.17''$). The test data in the right part of Figure 20, where the image quality is worse than $2''$, show the image quality at the beginning of the tracking. Another test example was performed on 2008 December 16, also with good seeing conditions of in Xinglong; the acceptance testing group performed a test by tracking a star for 3 h with declination angle 57.03°. The best image size was $0.198''$, in terms of E80%, corresponding to an estimated FWHM of $0.13''$.

During the test, it was easy to notice that even though the image measured by the S-H wavefront sensor could eliminate most of the effects of air turbulence, the accuracy of the image results still depended on the seeing conditions. We believe that at a better observation site, an even better image quality could be achieved by using the active control of the LAMOST optical system.

Test result by guiding cameras There are four guiding cameras located on the focal surface with a FOV of 3.2° in diameter, for guiding the telescope and calibrating of the coordinate system of the optical fibers and scale of the focal surface. With these CCD cameras, we can acquire information on image quality including the influence of the seeing and tracking error.

In Figure 21, one image with FWHM of about $2''$ was obtained by a guiding camera, but the image quality tested by the S-H wavefront sensor is about $0.3'' \sim 0.4''$, and seeing is about FWHM $1.7'' \sim 2''$.

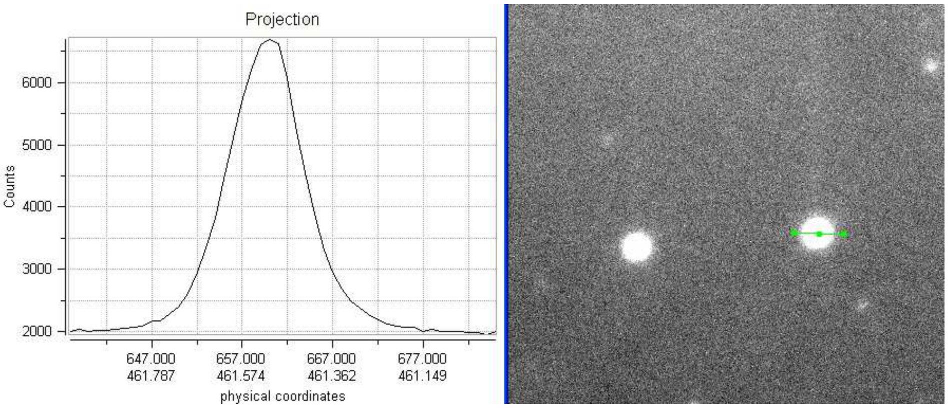

Fig. 21 Image is 2′′ FWHM obtained from the guiding CCD with a field of view of 3.2° in diameter.

2.13 Pointing, Tracking and Control System

The pointing and tracking system consists of two parts: 1) the alt-azimuth mounting (Fig. 22) of Ma for pointing and tracking the objects; 2) The focal mechanism for the focal surface derotation and focusing of the optical system (Fig. 23). These two parts are mainly composed of components such as hydrostatic bearings, friction drives, tape encoders, counter torque balancing system, field derotation mechanism, focusing unit, and focal surface attitude control system (Li et al. 2003).

The mounting and tracking system of LAMOST has some special characteristics:

1) There is no blind area for LAMOST.
2) There is no gravitational deformation of Mb since it is fixed.
3) The observations are around the meridian, due to the special pointing and tracking mode, and changes in the altitude are very small during the tracking process; therefore the gravitational deformation of the structure caused by the change of gravitational direction is very small. For example, in 1.5 h of tracking, the change in the altitude axis is only 0.34° (for the worst case).
4) A friction drive is employed for both elevation and azimuth axes for reducing the high frequency tracking errors.
5) Because the tracking follows a normal line, the technical requirements in pointing and tracking are twice as strict as for an ordinary telescope, and the size of the azimuth drive platform is about 8 m in diameter, which is much larger than normal telescopes with the same size aperture.
6) LAMOST has adopted a special counter torque gear system to balance the load on the altitude axis since there is not a normal telescope tube to do the balancing like in a traditional telescope.

The control system (Yang & Zhang 2008) mainly consists of three subsystems: (1) the tracking and driving system of the alt-azimuth mount for Ma, the rotation of the focal surface as well as the guiding star system. (2) The control system of the thin mirror active optics and the segmented mirror active optics with approximately 1000 force actuators and displacement actuators. (3) The system of real time environmental monitoring, control, and fault-diagnosis including the dome control, temperature monitor, the wind screens and the control of the ventilation windows, the rain and dew monitor and control, the alarm facilities, the remote monitor and control etc. Its characteristics can be summarized as follows: (1) Having the system features available during real time, with reliability, network availability, multilayers, and being distributed and expandable, like in other modern

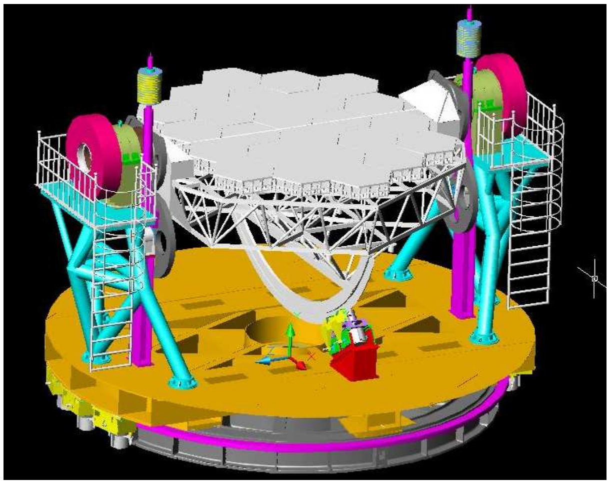

Fig. 22 Ma and its alt-az mounting and tracking structure (computer model).

Fig. 23 *Left*: Ma mounting and tracking structure being assembled; *Right*: the focal structure being assembled.

large astronomical telescopes around the world. (2) Controlling the thousands of force actuators and displacement actuators with high precision, and collecting and analyzing the signals from thousands of force actuators and displacement actuators in real time.

For LAMOST, the accuracy required for pointing is $10''$ and that for tracking is smaller than $0.64''$ on the focal surface. It means $5''$ for pointing and $0.32''$ tracking for the normal line of Ma. The final test by the CCD cameras on the focal surface for pointing and tracking stars is shown in Figure 24, with all results meeting the design requirements. Below are listed the operational parameters and accuracy requirements for the alt-azimuth mounting and focal unit. The final test results have shown that all are met and some are even exceeded in LAMOST.

1) Ma altitude tracking range: $\pm 2^\circ$
2) Ma altitude rotation range: 0∼90°

3) Ma azimuth rotation range: ±51°
4) Ma azimuth tracking range: ±20°
5) Pointing accuracy: less than $10''$ (on the focal surface)
6) Tracking accuracy (with guiding): less than $0.64''$ (on the focal surface)
7) Focal surface rotation: ±22.5° with an accuracy of $\pm 1''$
8) Focusing: ±200 mm with an accuracy of 0.1 mm (0.02 mm in the final test)
9) Focal surface attitude: $0 \sim 10'$ with an accuracy of $\pm 10''$
10) Focal unit lateral movement: 2.2 m with an accuracy of ±0.02 mm

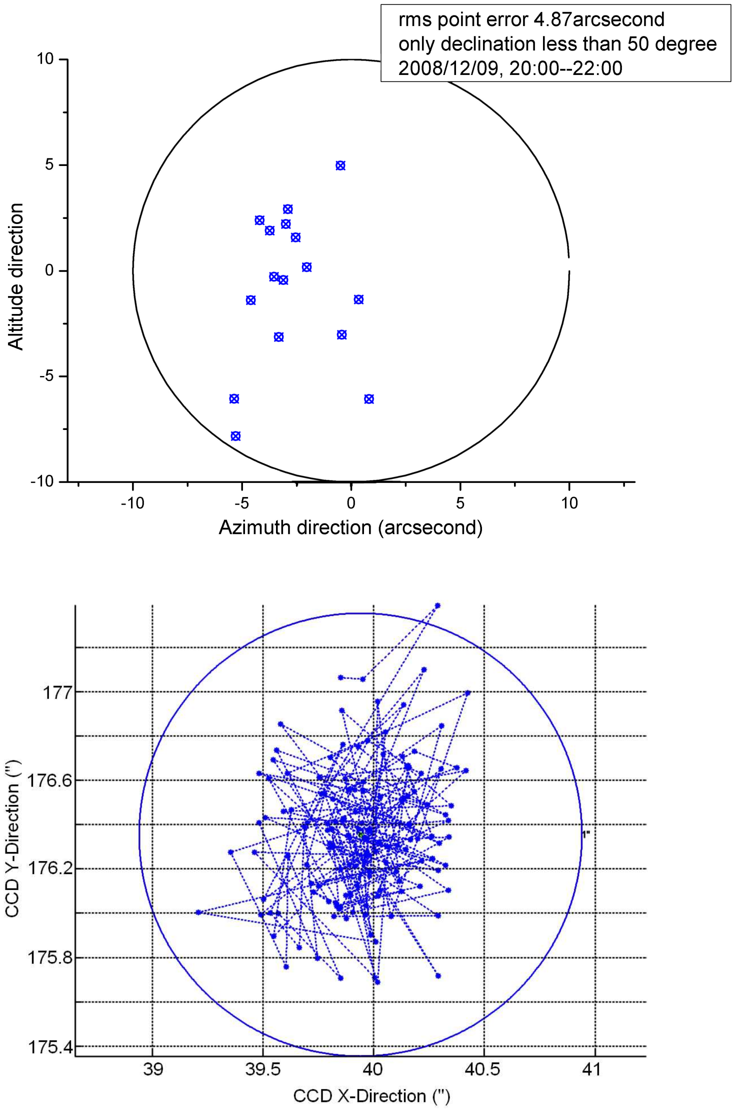

Fig. 24 *Top*: result of pointing $(4.87'')$ on 2008 Dec. 9; *Bottom*: result of tracking $(0.42'')$ on 2008 Nov. 19.

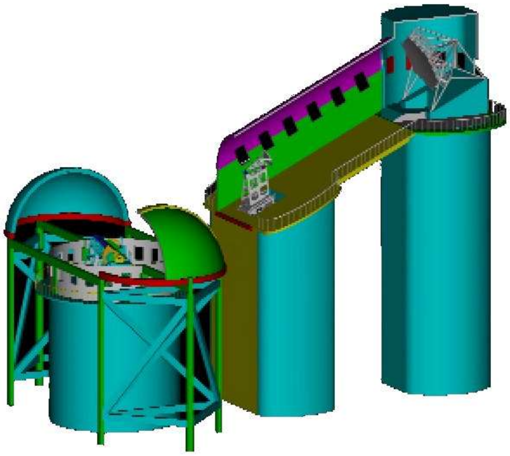

Fig. 25 Enclosure of LAMOST with an open dome, tunnel enclosure with louvers, circular wind screen of Ma with louvers and six active wind screens.

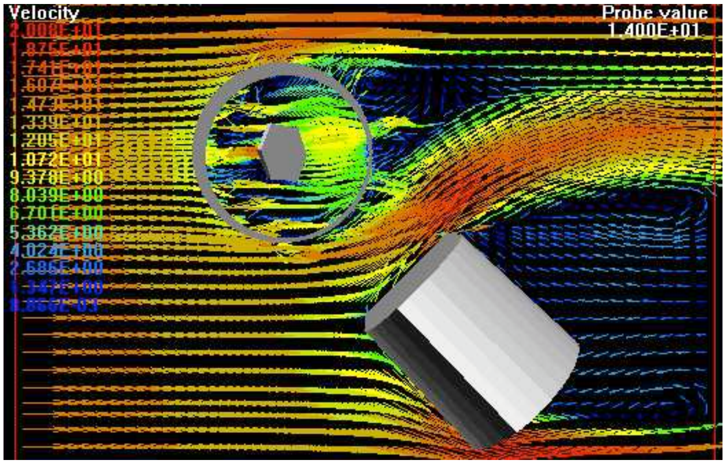

Fig. 26 The numeric simulation for optimization of the enclosure.

2.14 Enclosure, Wind Buffering and Thermal Control

LAMOST's enclosure is unique. The design of the dome incorporates a completely open mode during observation for Ma and a tunnel enclosure from Mb for focusing (Fig. 25) (Yao et al. 2000).

For protecting the correcting mirror Ma from the heavy wind load, a wind tunnel test has been done (Yao 1998) and a numerical simulation for optimization has been carried out (Yao et al. 2000) (Fig. 26). From the wind tunnel test and optimization calculation, a fixed circular wind screen around Ma and six active wind screens to the north of Ma have been applied, with the specification that LAMOST could be in normal operation if the wind speed is not higher than level 5 on the Beaufort scale. The circular wind screen has been designed so that it can reduce the wind load from level 5 to level 3 on the surface of Ma. Under the conditions of wind level 3, there should be no obvious image distortion by wind load deformation and no vibration of the mirror or the support system (Yao

1998). In some cases when the wind is too strong in the north direction, the active wind screens can be raised for increased protection.

The optical axis of the primary mirror (Mb) in LAMOST is fixed and tilted 25° downward with respect to the ground. The optical path is 60 meters, much longer than that of a traditional telescope. The temperature difference between the inside and the outside of the enclosure and gradient around the structure causes dome seeing and thermal distortions in the telescope structure. The outside temperature always decreases faster than the inside temperature during the observation. To ensure good dome seeing, a cooling system should be used. A numerical simulation has been done to model the temperature distribution under cooling (Hao 2004; Yao et al. 2003). The results of the simulation showed the temperature difference between the focal surface and environment was 1.05 °C lower than without cooling after one hour if the wind speed did not exceed $1\,\mathrm{m\,s^{-1}}$.

The cooling system in LAMOST requires cooling air a maximum of 5 °C lower than the environment, to keep the temperature difference between the inside of the enclosure and the outside nearly the same during the observation. The lowest temperature in winter can reach –30 °. The temperature can be adjusted by a computer control system according to the thermal monitoring system. There are three cooling modes in LAMOST: (1) cooling the entire inside space of the enclosure: (2) cooling the floor of the enclosure to let the temperature be a little lower on the floor; (3) cooling the local heating sources such as motors and electronics when needed.

There is a ventilation system used to reduce the air temperature gradient inside enclosure, to let the temperature inside the enclosure be close to that of the outside, and to keep a smooth airflow for better enclosure seeing. There are five fans with power 80KW, to let air outside of the enclosure move along the optical axis during observing. The speed of the resulting air flow is adjustable in the range of about $1\text{–}2\,\mathrm{m\,s^{-1}}$. In the wall of the enclosure there are louvers, and when wind speed is suitable, the open louvers can be used for natural ventilation.

The thermal monitoring system in LAMOST is composed of temperature sensors, temperature measurement instruments, a network of computers to collect data and a central controlling computer. There are also many electronics that can produce electromagnetic interference. In order to obtain a precise measurement of temperature, hardware and software anti-jamming means are used. There are about 300 temperature sensors distributed on the back sides of mirrors, truss structure of Ma and Mb, on the focal surface panel, on the pier, and in the enclosure tunnel. With this monitoring system, one can survey the temperature of the truss and mirror support systems of Ma and Mb, and also measure the temperature in the enclosure and on the focal surface. Using this system, we can monitor the temperature gradient of the system, so as to control the cooling and ventilation systems to get temperature uniformity in the enclosure. The resolution of the temperature monitoring system is 0.02 °C, precise up to 0.05 °C.

During 2000 to 2004, some experiments of the above ventilation and cooling methods for the LAMOST enclosure were carried out, together with the experiment for active optics on the 1m LAMOST experiment telescope in NIAOT. The experiment's results showed that with proper thermal monitoring, and with ventilation and a cooling systems being applied, the enclosure's seeing could be significantly improved.

3 INSTRUMENTS

3.1 Fiber Positioning System

3.1.1 Introduction

The fiber positioning system on the focal surface is an important part of LAMOST. All of the 4000 fibers must be positioned on the 5° focal surface precisely and quickly. The main technical requirements of the LAMOST fiber positioning system are described as follows:

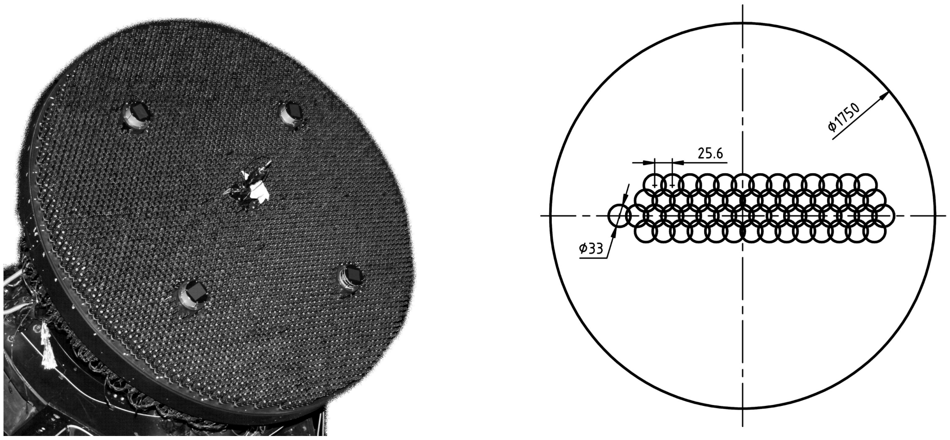

Fig. 27 *Left*: the fiber positioning system on the focal surface; *Right*: distribution of fiber positioning units.

1) The 2D positioning error of any one of the 4000 fibers should be less than 40 microns (with respect to $0.4''$ in the focal surface).
2) The time needed for positioning all the 4000 fibers at one time should be shorter than 10 min.
3) During observation, errors should be compensated.

Before LAMOST, spectroscopy telescopes used two kinds of fiber positioning methods: one is a holing method, and the other is a magnetic plotter method. The SDSS project uses the holing method (Gunn & Knapp 1993). This means before each observation, the focal plate must be drilled with a lot of holes according to the positions of objects, then the fibers need to be plugged into the holes. After each observation, one must change the focal plate and unplug the fibers to prepare for another observation. Another way is using magnetic plotter units. Each unit has three parts: a reflecting mirror, a magnetic iron, and one fiber. The focal plate is made of iron. At each observation, each magnetic unit is positioned in the right place for the object. After the observation, a robot will take the unit and place it at the next position. This method is used in the 2dF project (Jones 1994). To increase the efficiency of changing units, there are ten robots to do the job.

The holing method could not be used in LAMOST because in this method, after each observation, one should pull out the fibers from the focal surface and plug them in to the next position on the focal surface. The time needed is about half an hour for SDSS, but it would be at least one hour for LAMOST.

In the magnetic plotter method, the fibers are placed on the focal surface, as in 2dF with thin fibers, with a low density of units, in such a way that they do not interfere with each other. LAMOST, however, uses thick fibers and the density of the fibers is higher than those in 2dF. In this case, LAMOST would need twice as much area for the focal surface to place the fibers. It would also need a long time for preparation before each observation, so this method is also not suitable for LAMOST.

There is a new kind of fiber positioning system designed for LAMOST (Xing et al. 1998), named the distributive parallel-controllable fiber positioning system (the left panel of Fig. 27). The focal surface of the telescope with a diameter of 1.75 m is divided into 4000 individual domains (the right panel of Fig. 27). Each domain contains a controllable unit which can move a fiber quickly anywhere within its designated circular area on the focal surface. A mobile parallel control system is set to control all the units, so the 4000 fibers can all move separately. In this system, the positioning errors

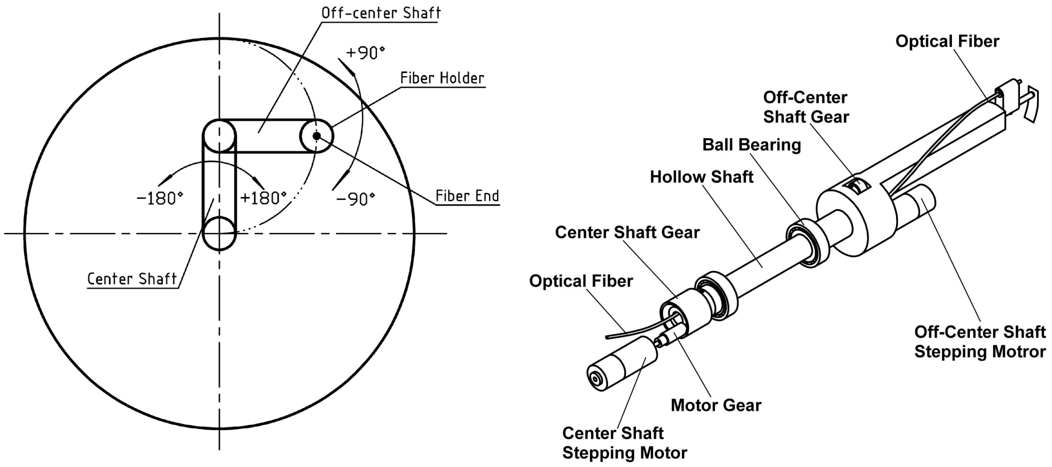

Fig. 28 *Left*: the double revolving fiber positioning unit; *Right*: schematic of the structure of the unit.

can be compensated during real time, and the preparation time for each observation is shortened to several minutes.

3.1.2 Design of the fiber positioning system

The fiber positioning system consists of a base plate (the focal survey), 4000 fiber positioning units, an electronic control system and equipment that measures the positions of fibers. Each unit can position its fiber within the range of $\phi 33$ mm, and the distance to the nearest unit is 25.6 mm. The circular domains are overlapped to ensure that there is no blind space on the focal surface. Each unit is driven by two stepping motors and controlled by computer in such a way to ensure that the units do not collide with each other.

Double revolving fiber positioning unit The principle of double revolving fiber positioning is shown in the left panel of Figure 28. The unit contains a central shaft which revolves around its fixed end in a range of $\pm 180°$, and an off-center shaft which revolves around its end that is connected to the free end of the central shaft. The fiber which is installed on the free end of the off-center shaft could then be moved to anywhere within its designated circular domain of the focal surface when the lengths of the two shafts are exactly the same. The schematic drawing of the fiber positioning unit is shown in the right panel of Figure 28. The lengths of the central shaft and the off-center shaft are all 8.25 mm, to cover a positioning area of $\phi 33$ mm.

The central revolving shaft is driven through a precision gear pair by a stepping motor with reducer of 1:1024, and the off-center revolving mechanism is driven by a stepping motor with reducer of 1:16. In order to fulfill the required positioning precision, some special technologies were developed to improve the positioning accuracy. For example, a friction mechanism was developed for eliminating the return error of the central shaft gears, and single-side-contact using a spring was developed for the off-center shaft gears. Two types of highly sensitive electro-mechanical position sensors were developed to set starting points for the two shafts, as the absolute positioning fiducial point.

The systematic errors of rotation angles of the two shafts were carefully measured and saved as a database in the main control computer. It has been confirmed that with the real time compensation

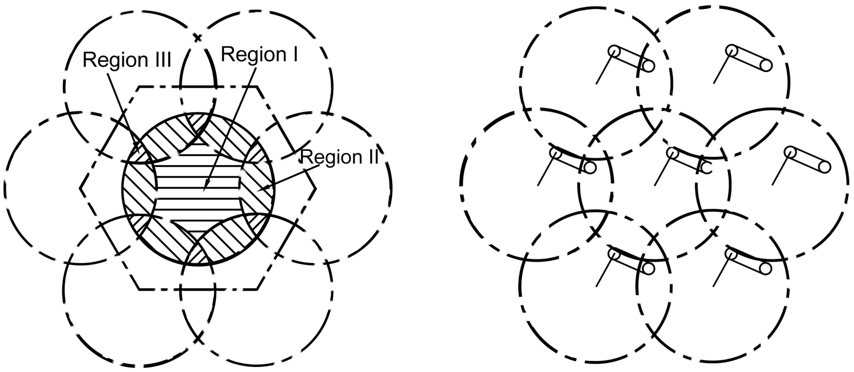

Fig. 29 *Left*: Three types of regions involved in the observation. *Right*: Sketch map of preparatory processing.

of the systematic angle errors, and the positioning accuracy of all the units within their full range are less than 40 microns.

Control system based on a Zigbee wireless communication network The control system is designed for the 4000 fiber positioning units with a multi-layer control structure. The first layer is the LAMOST main computer, the second layer is the control computer of the fiber units, the third layer is the control units connecting the mechanical units, and the fourth layer is the motor driver and the motor.

The communication of control commands from the control computer to the control units was implemented through a Zigbee wireless communication network. Combining the advantages of low power consumption, low cost and low data rate, the technology of Zigbee wireless communication, which follows the IEEE802.15 standard, can meet the needs of most network topology models because it supports star networks, cluster tree networks and mesh networks.

3.1.3 Route planning for fiber movement

According to the arrangement of fiber positioning units, the observing domain of one unit can be divided into three regions (the left panel of Fig. 29). The objects in region I can only be observed by one unit, the objects in region II can be observed by either unit, and the objects in region III can be observed by any one of the three units. Because the objects in region I can only be allocated to one unit, they should be allocated first. Then objects in regions II or III are allocated. There are two basic rules that allocations should follow. The first is that allocations should make the number of objects as large as possible. The second is when two units have the same number of objects that have been allocated, objects should be allocated to the one which is nearer to them, in order to reduce the probability of mechanical collisions during observation. The leftover objects are allocated finally, and these allocations still obey the same two rules above.

After the allocations of objects, the paths of movement for all units and the order of observations must be planned to avoid mechanical collisions. The goals of planning are: collision avoidance, higher fiber usage efficiency and higher total observation efficiency. Before collision detection and processing, the objects to be observed in every unit can be arranged by the order of the central shaft angles from small to large. This preparatory processing makes the arms of different fibers point toward almost the same direction during one round of observation. The right panel of Figure 29 is an example. This leads to fewer mechanical collisions during observations. As a result, the loss of efficiency due to fiber collisions can be decreased beforehand.

3.1.4 Measurement of positions of 4000 fibers

In a fiber positioning system, geometrical coordinates of fibers need to be measured in order to verify the precision of fiber positioning. A measurement system based on a CCD camera was constructed. A standard spot array is used to calibrate the coordinate of the camera with high precision. Fibers installed in the positioning units are illuminated from their other ends. When the fibers move to a point, its position is measured by the camera. The coordinate parameters in the focal surface of 4000 positioning units can be obtained by measuring a series of positions for each fiber.

After finding the coordinate parameters of 4000 positioning units in the focal surface, the link between the coordinates of the focal surface and the celestial coordinates is needed. The displacement of a fiber from an object is measured by the “fiber scan” method. The method measures the flux changes of objects passing through the fibers when the telescope points to different positions around the center of a sky field. The displacements of 4000 fibers can be used to build a coordinate relation between the focal surface and celestial coordinates.

3.2 Spectrographs

3.2.1 Introduction

The 16 low resolution spectrographs are the main survey instruments of LAMOST. Those spectrographs have been put into operation at Xinglong station since late 2008 (Zhu et al. 2011, 2006; Hou et al. 2010). The spectrographs can obtain specta of 4000 celestial objects simultaneously via fibers with $3.3''$ diameter located in the 5° FOV of the telescope. The wavelength range of each spectrograph is from 370 nm to 900 nm, and spectral resolution is 1000 or 5000, depending on when different gratings and camera positions are used. The resolution of the spectrographs can also be enhanced to 4000 or 20 000 by limiting the fiber slit to 1/4 slit width for a low or medium grating mode. The throughput of the spectrographs is better than 30%.

3.2.2 Design of the spectrographs

There are a few designs for multi-object fiber fed spectrographs (Uomoto et al. 1999; Saunders et al. 2004; Smith et al. 2004; Byard & O’Brien 2000). The LAMOST low resolution spectrographs have a double-beam full Schmidt design that uses volume phase holographic (VPH) gratings.

The layout of the optical system is shown in Figure 30. It consists of one f/4 Schmidt collimator, a diachronic beam-splitter, four VPH gratings, two articulating red and blue f/1.3 Schmidt cameras, and a field lens near the focal plane at the vacuum window of the CCD detector’s cryogenic head. Each spectrograph accommodates 250 fibers that are 320 microns in diameter (corresponding to $3.3''$). Beams that enter the spectrograph are of f/4 due to fiber degradation. The 200 mm diameter collimated beam is split into two separate channels. The blue channel is optimized for 370–590 nm, and the red channel for 570–900 nm.

Spectrograph specifications Each spectrograph is articulated to work in low or medium resolution mode. Tables 4 and 5 list the resolution of each mode. The VPH gratings work at angles near the blaze angle. The R number is larger than $3200''$. This means each spectrograph scale is very large due to the seeing conditions. The scheduled collimating beam size is 200 mm. By limiting the entrance width of the slit placed at the end of the fiber, spectral resolution is doubled. The spectrographs are designed for spectral resolution power 1000 (4000) and 5000 (20 000), with multi-object capability. The actual wavelength coverage is 365 – 900 nm. The wavelength of the peak efficiency can be tuned a little due to the super blaze property of the VPH gratings.

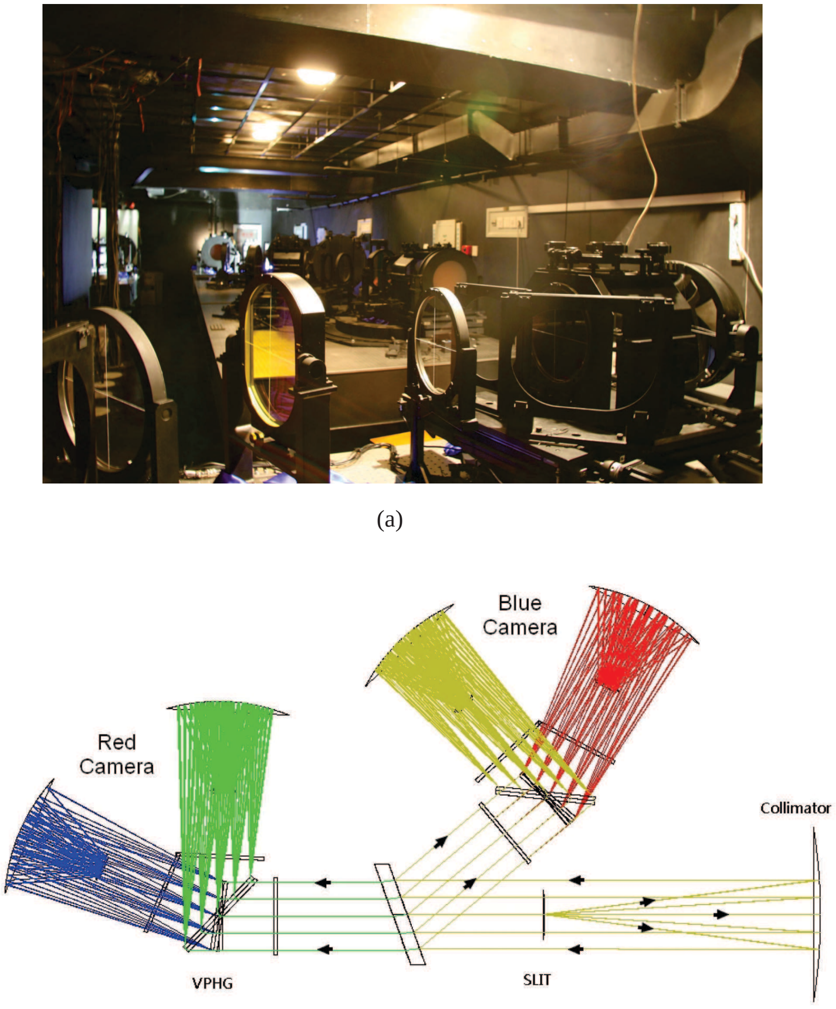

(a)

(b)

Fig. 30 Layout of the low resolution spectrograph optical system.

Table 4 Resolution of Low Resolution Mode

	Blue Arm		Red Arm	
	Wavelength (nm)	Resolution	Wavelength (nm)	Resolution
Full slit	370 – 590	1000	570 – 900	1000
1/2 slit	370 – 590	2000	570 – 900	2000
2/3 slit	370 – 590	1500	570 – 900	1500
1/4 slit	370 – 590	4000	570 – 900	4000

Grating sets of the spectrographs VPH gratings for low and medium dispersion respectively afford higher flux and more flexibility compared with ordinary surface relief gratings (Barden et al. 1998).

Table 5 Resolution of Medium Resolution Mode

	Blue Arm		Red Arm	
	Wavelength (nm)	Resolution	Wavelength (nm)	Resolution
Full slit	510 – 540	5000	830 – 890	5000
2/3 slit	510 – 540	7500	830 – 890	7500
1/2 slit	510 – 540	10 000	830 – 890	10 000
1/4 slit	510 – 540	20 000	830 – 890	20 000

Table 6 Grating Sets of the Spectrographs

Gratings	Grating 1	Grating 2	Grating 3	Grating 4
Number Of Units (Pcs)	16	16	16*	16*
Spatial Frequency (lp mm)	540	800	1680	2750
Wavelength Range (nm)	570 – 900	365 – 590	830 – 890	510 – 540
Center Wavelength (nm)	740.46	480.38	862.65	526.25
External AOI (°)	8.63	8.17	43.9	43.9
External AOD (°)	14.46	14	49.1	49.1
Physical Dimensions (mm)	220×220×20	220×220×20	310×220×22	310×220×22
Resolution	1000 – 2000	1000 – 2000	5000 – 10 000	5000 – 10 000

Notes: ∗ Only one set of medium resolution gratings is installed at the current stage.

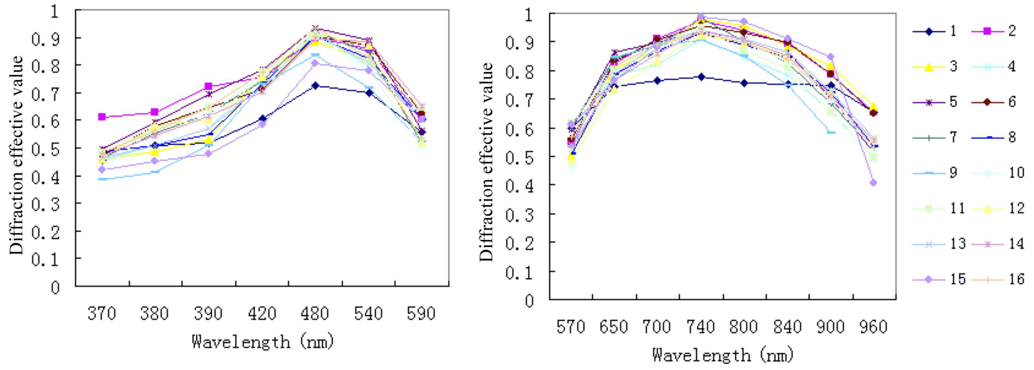

Fig. 31 Efficiencies of 16 VPH gratings. *Left*: Blue channel; *Right*: Red channel.

Table 6 shows the grating sets of the low resolution mode and the medium resolution mode. Efficiencies of VPH gratings are shown in Figure 31. Those gratings are delivered in different batches which show a variation in efficiency. The efficiency of the blue channel gratings is around 80%. The efficiency of the red channel gratings is around 90%.

3.2.3 Performances of the spectrographs

The 16 spectrographs used in LAMOST are in low-resolution mode with 2/3 slits. The spectral resolution power is $R = 1500$. In the future, one can change the spectral resolution by replacing gratings or slits.

The throughput was defined as the ratio of the number of photons entering the spectrograph slit to the number of the photo-electrons detected by the CCD. The efficiency of each spectrograph was measured with a monochromator and a silicon detector. Figure 32 shows the throughput of the red

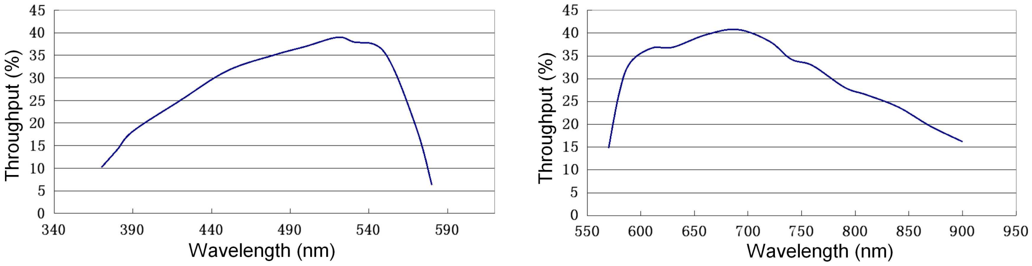

Fig. 32 Efficiencies of 16 VPH gratings. *left*: Blue channel; *Right*: Red channel.

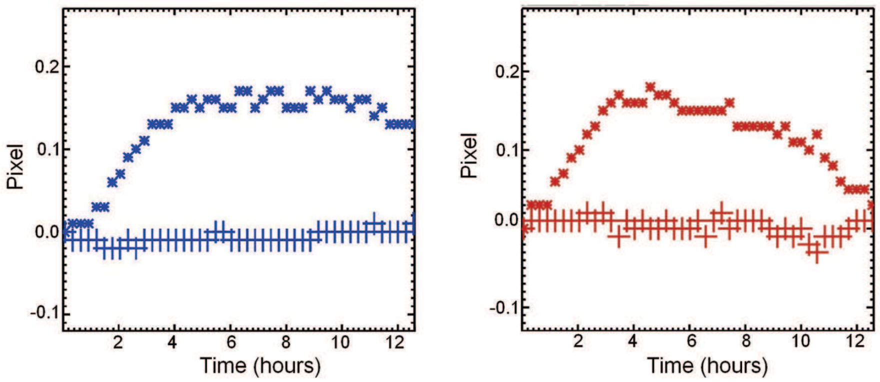

Fig. 33 The measured image shift along the dispersion direction (+) and along the space direction (*) in 12.5 h. The abscissa axis represents 12.5 h, and the ordinate axis represents image movements in pixels.

and the blue channel of one spectrograph. The throughput of the telescope, fiber, slit and CCD is not included.

The LAMOST science objective requires that the radial velocities of stars be measured to a relative accuracy of 4 km s^{-1} over the entire 5° FOV within 2 h. This requirement results in the specification of image movement of the spectrograph being less than 0.6 μm/h (0.05pixel/h).

Figure 33 gives the measured image shift along the dispersion and along the space direction in 12.5 h. The image shift is measured from the arc spectrum that was exposed for 12.5 h.

3.2.4 CCD cameras

A spectrum of a light beam from fibers (arranged along a slit with height of 144 mm in front of each spectrograph) is imaged onto 32 cameras each with a 4096×4096 EEV CCD chip and a square pixel size of 12 μm (Zou & Wang 2006; Wei & Stover 1996). The full width half maximum (FWHM) of monochromatic images is about 7–9 pixels. Dispersion of the red band is about 0.084 nm pixel^{-1}, and the dispersion of the blue band is 0.057 nm pixel^{-1}.

The 32 CCDs, used for low resolution spectrographs, are EEV CCD203-82 scientific CCD sensors with different coatings. Figure 34 (top) shows typical quantum efficiency curves of the blue channel CCDs and of the red channel CCDs. The 49.2 mm× 49.2 mm imaging area of a chip has flatness better than ± 15 μm with a 100% active area. The back-illuminated spectral response, com-

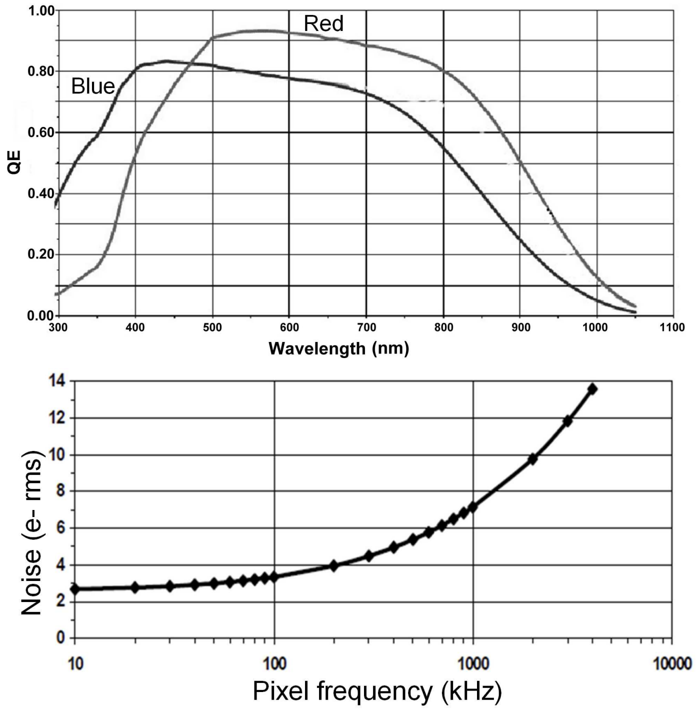

Fig. 34 *Top*: Typical quantum efficiency of CCDs; *Bottom*: Typical output amplifier noise of CCDs.

bined with very low read-out noise, gives exceptional sensitivity. There are extra rows of pixels such that the total number is actually 4096 horizontal by $2\times$ 2068 = 4136 vertical. The register and output capacities are designed to allow full capacity 2×2 binning, so that the device can be operated efficiently as a 2048×2068 imager with 24 μm pixels.

Figure 34 (bottom) is its typical amplifier noise curve with respect to reading speed. The performance (at 173 K unless stated otherwise) of the CCD cameras is as follows:

	Min	Typical	Max	Units
Peak charge storage (image)	130 000	175 000	–	e^-/pixel
Peak charge storage (register)	–	750 000	–	e^-/pixel
Readout noise		3	4.5	e^-rms
Readout frequency	20	50	3000	kHz
Dark signal				
At 173 K	–	3	–	e^-/pixel
At 153 K	–	0.01	2	e^-/pixel
CET				
Parallel	99.9990	99.9995	100	%
Serial	99.9990	99.9995	100	%
Spectral range	300	–	1060	nm
Peak QE	–	90	–	%

4 SURVEY OPERATION

4.1 Survey Strategy System

4.1.1 Introduction

The scientific goal of the Survey Strategy System (SSS) of LAMOST is to carry out an effective observation program, determine the observation time and arrange the observation process.

LAMOST will take about three to five years to perform survey observations of several million celestial objects. A good observation program for LAMOST with 4000 fibers should have a higher fiber allocation rate so that a series of observation programs will use less observation times to meet a designated coverage rate on a large sky area. Each observation lasts 90 min for a given sky area and data are readout every half an hour. During the spectroscopic survey of LAMOST, SSS operates under many static and dynamic restrictions, trying to find a perfect observation position and allocates fibers to objects with the goal of assigning targets to a large number of fibers.

Where to point the telescope (plate center) and how to allocate the fibers (one plate) is the primary problem that SSS solves. We use several tiling methods for different situations, and simulations have demonstrated the feasibility and effectiveness of those methods. Different constraints listed in Hao et al. (2005) were considered when designing each tiling and fiber allocation method.

4.1.2 Tiling algorithm

To best utilize multi-fiber observations with LAMOST, the greatest density object-selection strategy is adopted in SSS. For an available sky area, a batch of objects to be observed is stored in a database and updated after every observed night. Searching for the tiling with maximum density is a major task of SSS. To achieve this goal, the maximum density algorithm, density gradient algorithm, the mean-shift algorithm and bright central star methods are used in SSS.

1) **Maximum density method** The basic idea of the maximum density method is to find the tile with the maximum object count by making a uniform tiling over a given sky area. By traversing all the tiles covering the sky area, a tile with the maximum object count will be found and the new observation program is to be made at this position.

   The only factor that affects the speed of this algorithm and accuracy of the process of finding the tile with maximum density is the observed sky area. The denser the covering of sky is, the higher the accuracy of finding the tile with maximum density becomes and the longer the time for calculation is. By contrast, the less strict the requirement becomes, the shorter the time cost will be and the lower the accuracy of finding the maximum tile becomes.
2) **Density gradient method** The density gradient method is essentially iterative. Based on a uniform covering, this method makes an estimate of object distribution and moves the tile to the direction which is expected to have a higher object density.
3) **Mean-shift method** The basic idea of the mean-shift algorithm is also iterative. As objects in the sky area are distributed freely, a density gradient is computed by using the difference in density of different positions. Vectors are used to describe the position of targets in the tile, and then it is provable that the sum of vectors will be set along the positive direction of the density gradient. Using that key conclusion and the method of the iterative calculations, by moving the center of the telescope along the sum of vectors and again calculating the new vector sum, and then iteratively moving the telescope center, the telescope will converge to a local peak in density. In order to maintain the goal of uniformity of the remaining area and to avoid neglecting some local maxima in areas where density varies in a complicated way, the algorithm will try to find a position with an overall greater density at the beginning of the iteration by making a quick

coverage with crude accuracy over the whole available sky area before performing the iteration (Ren et al. 2007).

4) **Bright central star** This is a tiling method requiring a bright star (namely brighter than magnitude 8) in the plate's center for the S-H detector used in active optics and four stars (brighter than magnitude 17) for four guiding CCD cameras. These central bright stars are selected from the Hipparcos catalog (Perryman et al. 1997), those that are binaries are rejected, then the focal plane is rotated a bit to find the proper guide stars inside the FOV of the four guiding CCD cameras. Guiding stars are selected from the GSC2.3 catalog (Lasker et al. 2008). Those central stars will be rejected if no corresponding guiding stars can be found. Since in some areas (e.g. low Galactic latitude), the central stars are more than enough to fully cover that part of sky, a step by step search is applied to reject those redundant bright stars and find the maximum coverage of that area (Yuan et al. 2012).

4.1.3 Fiber allocation method

After the plate center is determined by the tiling method, each object in the input catalog will be assigned a priority according to the scientific requirement, i.e. most important targets will have highest priority. Beyond those scientific targets, there should be five standard targets whose flux is known to establish calibration and 20 sky fibers reserved in each spectrograph for data acquisition. The targets used for flux calibration will be allocated with the highest priority compared to other targets. All the other scientific targets will be assigned by order of priority. If there are more than two targets of the same priority in the same fiber cell, the one closest to the center of the fiber cell will be selected to avoid collision with neighboring fibers. If one target can be reached by different fibers at the same time, the target will be assigned to the fiber with the least number of available targets within its fiber cell (Morales et al. 2012). The sky fiber will be assigned last, and those fibers that are not assigned to any target will be considered first; if there are less than 20 sky fibers per spectrograph allocated, the scientific fibers with lowest priority will be rejected and reassigned to blank sky until there are 20 sky fibers assigned.

4.1.4 Simulation

In order to estimate how many objects can be observed in a certain period of time, and to adjust the survey design accordingly, a five year survey simulation was implemented using SSS with the actual weather information (i.e. the observational time, moon phase etc.) of the Xinglong station of NAOC (Yao et al. 2012). 1 362 043 galaxies and 5 659 582 stars with r magnitude less than 18 were selected from SDSS DR8 catalog as the input catalog, and galaxies were given a higher priority than stars. The sky coverage and density map are shown in Figure 35. Those SEGUE stripes with width less than the LAMOST field were not counted in the simulation. The simulation used the bright central

Table 7 Summary of Simulation

Time	Target observed			Observational hours	Total plates observed	Scientific targets allocated per plate
	all	galaxies	stars			
$1^{\rm st}$ year	1 047 360	353 351	694 009	875	409	3151
$2^{\rm nd}$ year	1 744 094	570 081	1 174 013	655	711	3081
$3^{\rm rd}$ year	2 472 446	767 778	1 705 216	730	1065	2898
$4^{\rm th}$ year	3 008 734	910 808	2 097 926	721	1393	2700
$5^{\rm th}$ year	3 542 042	1 040 562	2 501 480	875	1787	2470

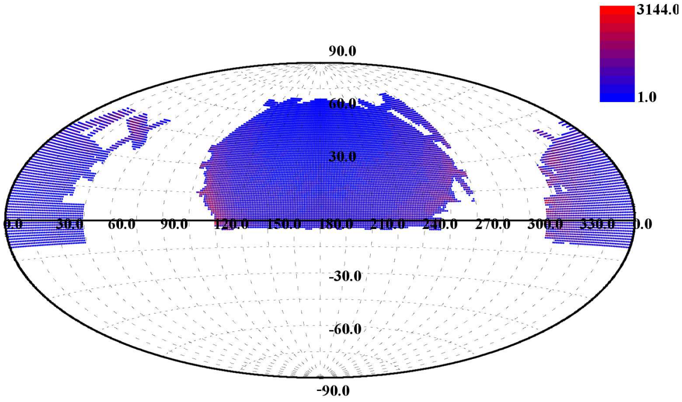

Fig. 35 Density map of the simulated input catalog. The unit of the color bar is number of objects per square degree.

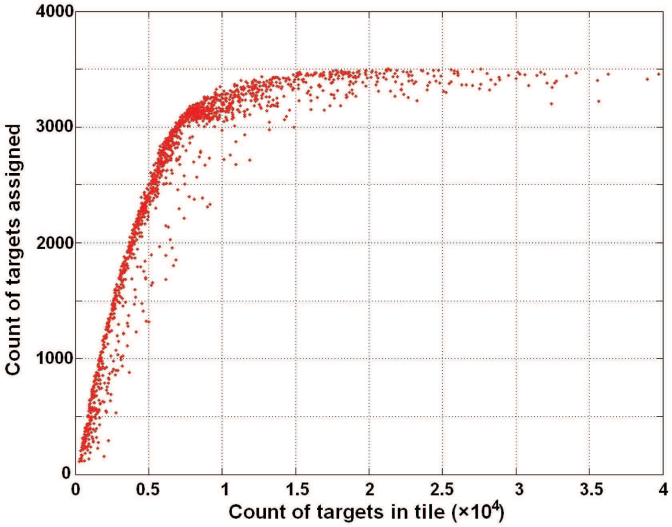

Fig. 36 Relationship between number of targets and the allocated fibers for one plate. The number of allocated fibers drops when the number of targets is less than 10 000.

star tiling method, scientific targets, sky fibers and fiber allocation method, which were described in 4.1.2.

The results are summarized in Table 7. Totally, 3.5 million targets were observed in a 5 year survey. 76% of galaxies and 44% of stars were observed. The targets observed per plate dropped yearly since target density dropped. Fiber allocation rate stayed high when the density of the input catalog was higher than 10 000 per plate (in 20 square degrees), as shown in Figure 36.

Figures 37 and 38 show the fractions of galaxies and stars observed respectively, with galaxies having a higher observational rate due to higher priority and lower density. Both galaxies and stars were less observed in the RA range of 210° to 240°, due to the seasonal weather and observational

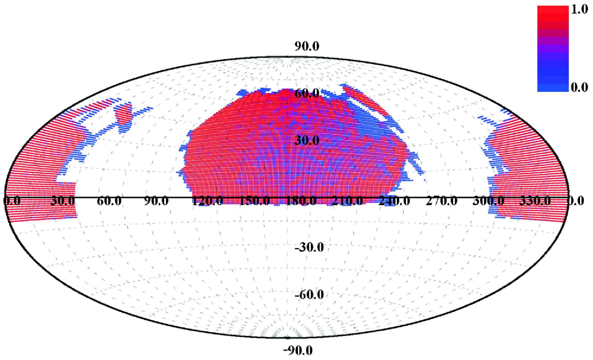

Fig. 37 Fraction of galaxies observed after a five year survey.

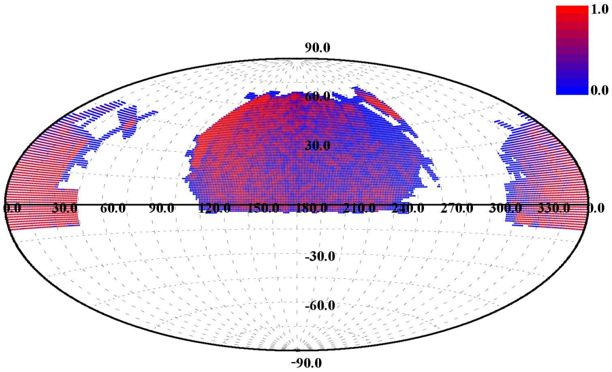

Fig. 38 Fraction of stars observed after a five year survey.

time change of the Xinglong station which becomes worse starting from April. This seasonal pattern can also be seen from the map of observed stellar fraction in Figure 38.

4.2 Observatory Control System

4.2.1 Introduction

The Observatory Control System (OCS) is one of the main systems in the LAMOST software (Zhao 2000). The highest level is OCS, the lowest level is the real-time system, and the middle level is subsystems of LAMOST which include the TCS (Telescope Control System), ICS (Instrument Control System) and DHS (Data Handling System). OCS operates the telescope in real-time during spectroscopic observations and handles the observational schedule through SSS and data processing through DHS (Fig. 39). The goal of OCS is to do the entire observing process automatically, and make the scientific process more efficient.

The main mission of OCS is managing, coordinating and controlling the operations of the telescope in a precise and orderly manner in accordance with the observation plan. OCS will be implemented with software and hardware components that interface between the telescope subsystems, and between the running modules. These interfaces will employ a multi-layer architecture that is both centralized and distributed.

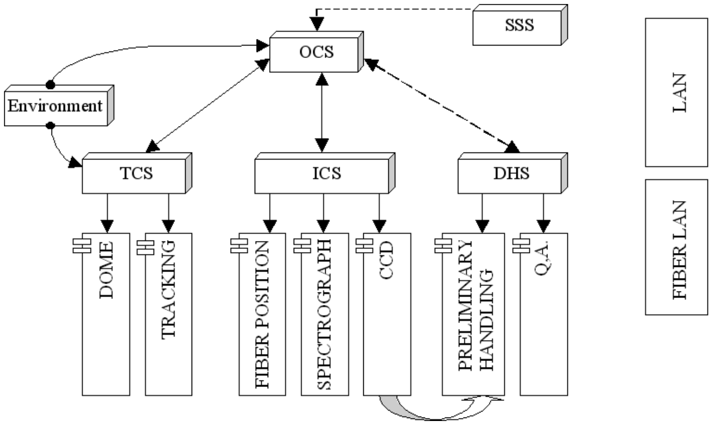

Fig. 39 LAMOST software system.

4.2.2 The development of OCS

To develop OCS, we have used modern software engineering technologies including the standard modeling language, Unified Modeling Language (UML) and its modeling structures, a reusable, object-oriented, component-and-framework-based approach to software-development (Wang et al. 2005).

The whole workflow of LAMOST is shown in Figure 40. Firstly, according to the science goals and sky survey strategy, the observation plan is generated by SSS, in which 4000 observed objects are selected from the database containing millions of objects (galaxies, quasars and stars). Secondly, OCS operates TCS and ICS in real-time based on the Observation Plan and Observation Process Flow during the observing night. The telescope Operation Reports and spectral Raw Data are recorded. Thirdly, the spectral Raw Data and spectral Quality Report are handled by the DHS. The Operation Report, Quality Report, and Analysis Report are also generated and sent to SSS for the next observation plan. The final data products will be released to collaborators for scientific research.

During the whole period of observation, every operation has its rules. Every operational command is send to SSS, TCS, ICS or DHS by OCS. When a command is received and accepted by a subsystem, the subsystem will execute the task and return the operational information to OCS. There are two kinds of sequences for basic execution of commands: parallel and serial. The parallel sequence is where the commands can be executed in parallel. The serial sequence is where the commands will be executed one after another. The whole sequence of observation commands, called the Observation Command Pipeline, is the combination of parallel and serial commands.

Communication between different OCS subsystems is important. When the system runs, OCS controls the process to make the whole observation automatic. OCS sends a command to the subsystem and the subsystem executes the command. At the same time, the subsystem must return the current status information to OCS. If an abnormality occurs, OCS will process it quickly to restore functionality.

The commands are classified as synchronous commands and asynchronous commands. If the command can be completed immediately, OCS will use it in a synchronous mode. If the command needs a period of time to complete, OCS will use it in an asynchronous mode. In OCS, most of the commands are asynchronous.

In order to guarantee that the command can be sent and executed normally, a command/status protocol, a command acceptance/rejection protocol and a command execution feedback protocol

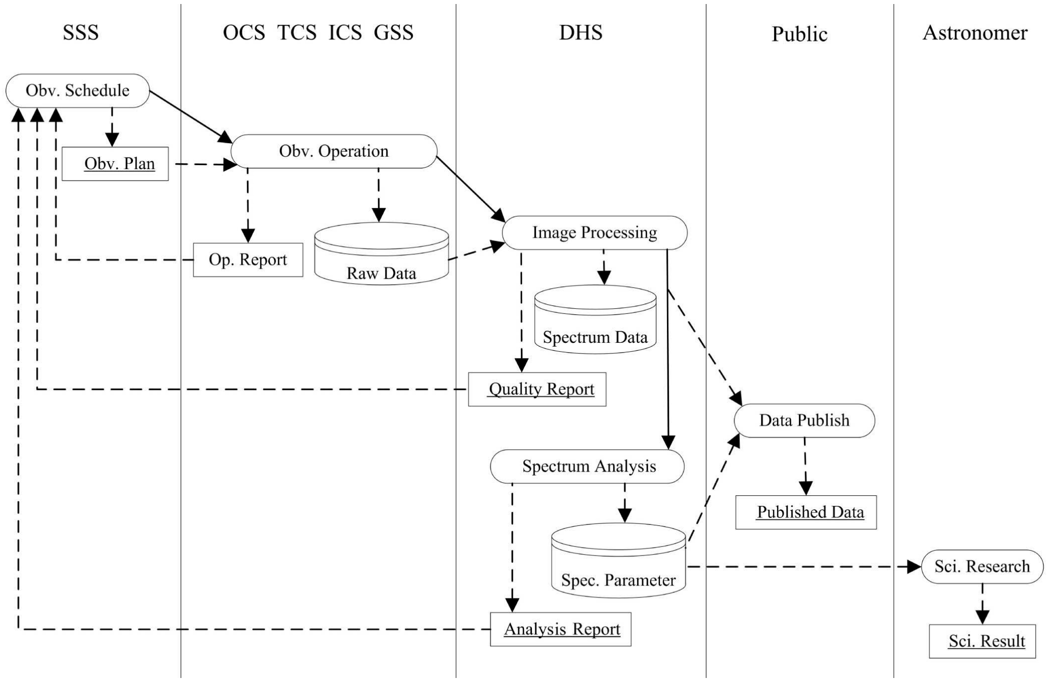

Fig. 40 LAMOST workflow.

between OCS and the various subsystems are defined. In an asynchronous mode, when the subsystem receives the command, it will simply analyze the command (including the command syntax scanning and command rule check), then decide whether to accept the command and return the result to OCS. If the command is accepted, it will return “0.” Otherwise, it returns a nonzero error code. The protocol can ensure that the command will be executed and not blocked.

The command execution feedback protocol makes the OCS respond more quickly. If all the information about the subsystem is not visible to OCS, OCS cannot efficiently monitor the execution status. The subsystem must send the execution information to OCS. There are six execution states when a command is executed: START, DONE, ERROR, ACTIVE, INTERRUPTED, and PAUSE, which are shown in Figure 41.

The status protocol includes errors, warnings and system information. If the change of status is random and unknown for OCS, there must be an approach to monitor and deal with the status. The subsystems have the responsibility to monitor the status and report the change to OCS. When OCS receives the change of status, it will generate an event and deal with the change of status.

The OCS is designed and implemented as a set of cooperating, distributed components that consist of objects. The objects in the system communicate based on the industry standard Common Object Request Broker Architecture (CORBA), which provides the communication infrastructure for the OCS. User interfaces use CORBA to communicate between themselves and with objects in the control and sequencing tier. CORBA objects act as wrappers for data servers providing public interfaces for local and remote user interfaces.

4.3 Data Reduction, Analysis and Data Products

The goals of LAMOST data reduction and analysis software are to reduce raw data, to classify spectra and to measure spectral parameters. The whole structure of the software was described in

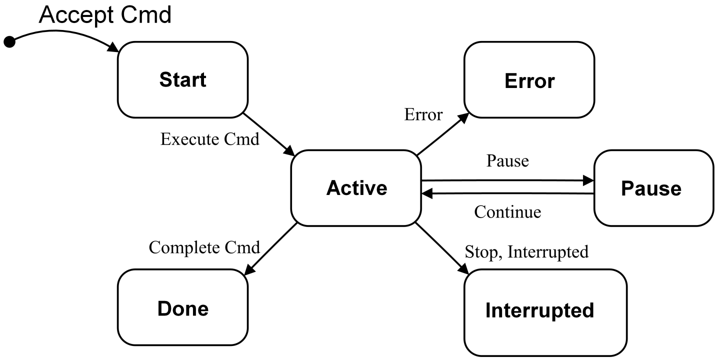

Fig. 41 The state machine for execution.

Luo et al. (2004). The input data of the data reduction software are raw CCD images, which are fed to the 2-dimensional (2D) Reduction Pipeline to be processed and extracted to 1-dimensional (1D) spectra. The output of the 2D pipeline is extracted and the calibrated 1D spectrum in the form of a FITS file is generated for each target. These 1D spectra are stored onto a hard disk array managed by a storage management server and indexed by a database system. The pre-processing procedure reads the 1D spectrum through standard I/O, and fits continua absorption and/or emission lines. Then, the spectrum is classified and measured by the 1D Pipeline by template matching and a line recognition algorithm. The output of the software includes two parts: one is calibrated spectra with parameters and analysis results written to FITS files, which are stored in the hard disk array, the other is FITS formatted catalogs, which record all information about the processed targets. All the data products will be stored in a database at the Data Center and released to the public.

4.3.1 2D pipeline

There are 16 spectrographs and two CCD cameras mounted on each spectrograph to record both red and blue images of multi fiber spectra. On each CCD image, 250 fiber spectra can be affected by the observing conditions.

The 2D pipeline of LAMOST aims to extract spectra from CCD images, and to calibrate them. The main tasks of the 2D pipeline include bias calibration, flat field, spectra extraction, sky subtraction, wavelength calibration, exposure merging and wavelength band connection.

The flat field is a very important process among all image processing steps. The focal surface of LAMOST is too big to easily correct differences in efficiency between fibers in the pipeline; it is currently using the fiber flat field to correct fiber to fiber differences inside the FOV of each spectrograph, since each of the 250 fibers mounted on the focal surface are located within about a 1° of FOV. Vignetting correction is also implemented by the fiber flat field procedure. The flat field processing will ensure equal efficiency of each fiber, which is related to the spectral extraction, accuracy of flux calibration and sky subtraction etc. Currently, LAMOST is regarded as 16 different instrument systems, and calibration of spectra is based on each separate spectrograph.

Extraction of spectra depends on the trace of the CCD image for each fiber. A good fitting of each spectral trace overcomes interference between different fiber spectra. The trace of each spectral flat field can be easily fitted by a polynomial, but it is difficult at both ends along the wavelength direction because of relatively low signal to noise ratio. To pick out signal pixels from background pixels is a key step of extraction and the pipeline fits each fiber profile by a Gaussian function in the spatial direction.

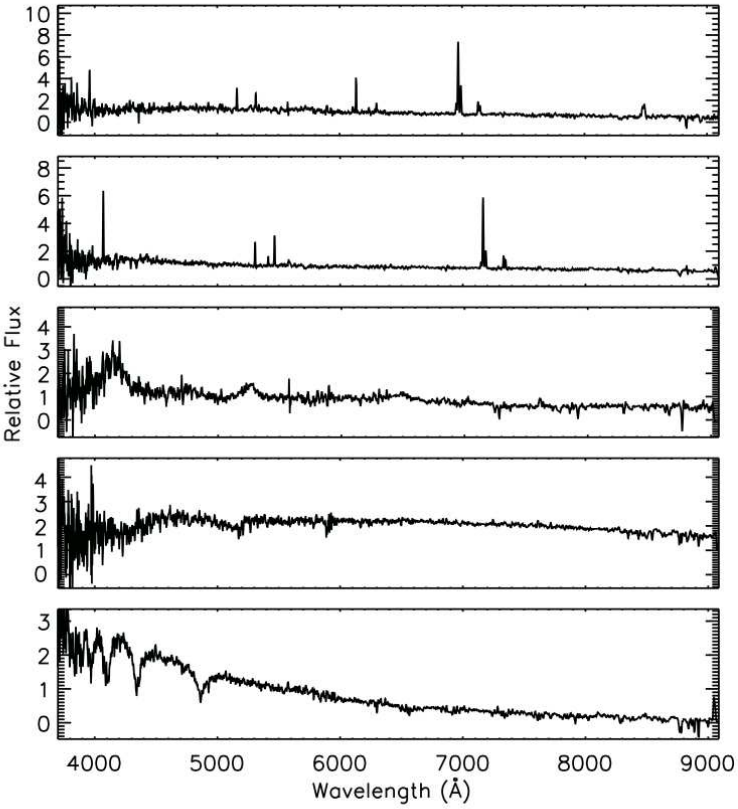

Fig. 42 The spectra of the LAMOST pilot survey. The top spectrum is an emission line galaxy with redshift 0.061, and its magnitudes of $ugriz$ are 20.30, 19.60, 19.90, 19.60 and 19.30 respectively; The second spectrum is also an emission line galaxy with redshift 0.09, and magnitudes of $ugriz$ are 20.10, 19.70, 19.90, 19.70 and 19.90 respectively; The third one is a quasar spectrum with redshift 2.40, and its magnitudes of $ugriz$ are 19.84, 19.21, 19.14, 19.18 and 18.97 respectively; The fourth spectrum is a K3 type star, and its magnitudes of $ugriz$ are 22.52, 20.37, 19.40, 19.17 and 19.11 respectively; The bottom one is a white dwarf spectrum, its magnitudes of $ugriz$ are 18.21, 17.89, 18.18, 18.42 and 18.64 respectively.

To achieve a limiting magnitude, many objects are fainter than their sky background, so one should carefully subtract the sky to reveal the spectra of those objects. Instead of moving the fiber to the sky position of each object, fixed fibers on each area are pointed to the sky and modelled by a supersky background for each spectrograph. If the sky is not well subtracted, the continua and lines of sky remnants will affect the subsequent spectral analysis. So several algorithms are used to subtract the sky, for example, PCA is applied to model the sky, and sky emission lines are used to correct differences in efficiency between sky fibers and object fibers.

The accuracy of wavelength calibration is decided by the dispersion curve which is fitted by a polynomial. With emission lines from wavelength lamps, the dispersion curve of each fiber is fitted. Then, the wavelength of each pixel can be calculated. To ensure high precision of wavelength, sky emission lines are also used in the pipeline to check the wavelength result. Figure 42 shows some spectra of the LAMOST pilot survey.

4.3.2 Online version of 2D pipeline

Online processing of a CCD image is a simple version of a 2D pipeline, but the algorithms used in the online version are not exactly the same as the 2D pipeline. The aim of the online procedure is to evaluate the quality and estimate the signal to noise ratio of the acquired spectra using in the DHS.

By using the online procedure, one can adjust the observation time in the next exposure. It is necessary to process the CCD image in real time. Whenever a CCD spectral image is acquired, the online processing will start, and the processing result will be given in several minutes. The quality of the acquired spectra could simply be judged by estimation of the signal to noise ratio and magnitudes of the objects.

FITS file packing is another important task of the online procedure. One FITS file of a CCD image produced by a camera only includes information about the exposure and CCD parameters. We need to record as much of the original information in the spectrum as possible. Thus, the online procedure has to collect a lot of related information from different subsystems of LAMOST, such as telescope control, focal surface, spectrograph, weather monitoring data, and guidance system status. Then, the information is fed into the FITS header as part of the raw data.

4.3.3 Spectral analysis pipeline

The spectral analysis pipeline of LAMOST includes continuum and line fitting, spectral classification and identification, measurement of spectral parameters etc. A one dimensional spectrum should be processed by first fitting its continuum and lines. This step is the basis of measuring spectral features in a spectrum. It is difficult to decide the physical continuum point in a low resolution spectrum for some kinds of objects, so the pipeline fits the so called global pseudo continuum to normalize the spectrum. For spectral line measurement, the local continuum for each line is also fitted by the pipeline. In the model of continuum fitting, the wavelet technique is used to derive a continuum in multi-scale to get the local continuum. For most spectra, noise affects the line measurement and local continuum fitting. Noise level varies with wavelength in a spectrum and local noise should be estimated for line measurement and some research work on modeling the noise has been carried out (Luo & Zhao 2001) and will be continued.

There are two kinds of spectral classification algorithms in the pipeline applied separately depending on the signal to noise ratio (SNR) of a spectrum. For low SNR spectra, some information from the input catalog has to be referenced to get the approximate type of the object, although it might be a false classification. Then, the spectrum is cross matched with all templates for identification. For relatively higher SNR spectra, a line measurement and identification algorithm is applied, For example, there are less than 1 percent of objects that might not be recognized correctly when SNR is higher than 10 (per pixel), and the details of the algorithm used in our pipeline are analyzed in another paper (Luo et al. 2012a).

No matter if line measurement or template matching classification are used, there are still some spectra that the pipeline cannot recognize by the above standard methods. Another data mining pipeline is available to identify spectral candidates of rare objects, such as cataclysmic variable stars or supernovae.

Measurements of redshift for extragalactic spectra and radial velocities for stars are also tasks for the pipeline. Two methods, template matching and spectral line shift averaging, are both used to get more precise velocity. The accuracy depends on wavelength calibration, spectral type and SNR of spectra. Theoretically, the accuracy of the velocity can reach one tenth of the instrument's resolution.

Another important task is to estimate stellar atmospheric parameters, e.g. effective temperature $T_{\rm eff}$, surface gravity log g, and metallicity [Fe/H], mostly for A, F, G and K type stars. The stellar parameters play significant roles for studying the formation and evolution of the Galaxy. These parameters are sensitive to some features in the spectroscopic data, thus the pipeline determines these parameters through measuring the specific features. However, these parameters do not act independently on an individual spectrum, e.g. degeneracies exists among temperature, gravity and metallicity, so there are several lines of research efforts with the goal of estimating stellar parameters from low resolution spectra. We have classified methods that are usually used in a reference (Luo et al. 2008).

Currently, three steps are employed to effectively determine those fundamental stellar measurements. Firstly, we utilize the relationship between the parameters and the line index features to approximately define the effective temperature range of the analyzed star, within a confidence interval $\pm 1000\,\mathrm{K}$. Secondly, based on the formerly fixed temperature scope, the pipeline automatically selects the appropriate stellar template fitting range, which includes features that are sensitive to the three parameters, then gives a set of the initial approximate values of the three parameters. Finally, we exploit ULySS (Koleva et al. 2009), which minimizes the χ^2 value between the observed spectrum and a multidimensional grid of model spectral parameters, where the model spectrum is generated by an interpolator (Wu et al. 2011b) built on the empirical ELODIE library (Prugniel & Soubiran 2001). We use this method to reliably determine the three fundamental parameters. Validation and precision of this method were illustrated in the work of Wu et al. (2011a). The details of the pipeline, result analysis, and error estimation will be published along with the data release of the data catalog for the LAMOST pilot survey (Luo et al. 2012a).

4.3.4 Data products

The LAMOST data archive will be distributed in two main forms: a set of spectroscopic objects and a set of individual spectra. The former will contain information on objects (such as spatial positions and photometric values), information related to the telescope and observations, line intensities (or equivalent widths), wavelengths of identified lines, identified types of all objects and measured parameters (such as redshifts or radial velocities, physical parameters etc). The latter will be comprised of one-dimensional spectra of observed objects.

The spectroscopic catalog is derived from headers in individual 1D spectra that record all information described above. The catalog is easily used by astronomers for their own researches, and a modern database of techniques ensure the highly efficient access to the catalog. There are also different sub-catalogs for peculiar objects which are picked out by the data mining method. Also for the 1D spectral dataset, each FITS file includes a calibrated spectrum and a normalized spectrum, which can be indexed and downloaded through the network. Under the data policy of LAMOST, the Virtual Observatory standard is introduced into the data publishing system.

Besides the spectroscopic catalog and spectral datasets, all algorithm modules we used in the pipeline could be provided to the public. Astronomers are encouraged to apply all these programs to their own research fields.

5 EARLY SCIENCES

LAMOST is a world-class survey instrument that is adaptable to a broad range of important astrophysical problems. The unique combination of a significant gain in multiplexing ability, wide FOV and large telescopic aperture will place LAMOST at the forefront of diagnostic survey spectroscopy in the next decade. It will provide astronomers with unrivalled research opportunities in Galactic and extragalactic astronomy.

Much progress has been made in the two year commissioning period to improve the performance of LAMOST systems, including fiber positioning, dome seeing control, and optical alignments of spectrographs on the hardware side; and calibrations, data pipelines and data archiving on the software side. LAMOST was already producing useful spectra in the commissioning period and has produced a number of scientific results, such as 17 new planetary nebulae discovered by Yuan et al. (2010) which are in the outskirts of the Andromeda Galaxy, 14 new background quasars discovered by Huo et al. (2010) which are in the vicinity of the Andromeda Galaxy, a very bright ($i = 16.44$) quasar discovered by Wu et al. (2010a) that is in the 'redshift desert' and eight new quasars discovered by Wu et al. (2010b), as well as eight new candidates of metal-poor stars discovered by Li et al. (2010) and another eight new candidates discovered in the pipeline for automatic determination of stellar atmospheric parameters (Wu et al. 2011a). LAMOST has also been used to research the kinematics and properties of stellar populations in the Andromeda galaxy (Zou et al. 2011).

The pilot survey of LAMOST was launched on 2011 October 24 and finished in 2012 June 24, as a test run of the whole system in survey mode in order to check the instrumental performance and assess the feasibility of the science goals of the LAMOST spectroscopic survey (Zhao et al. 2012). More than 677 000 spectra of objects are being released to Chinese astronomers and international collaborators (Newberg et al. 2012). A part of the pilot survey data, including about 319 000 high quality spectra with SNR$>$10, a catalog of stellar parameters of AFGK stars (Luo et al. 2012b) and another catalog of a subclass of M type stars (Yi et al. 2012), will be released to the public in August 2012.

References

Barden, S. C., Arns, J. A., & Colburn, W. S. 1998, in Society of Photo-Optical Instrumentation Engineers (SPIE) Conference Series, 3355, ed. S. D'Odorico, 866

Byard, P. L., & O'Brien, T. P. 2000, in Society of Photo-Optical Instrumentation Engineers (SPIE) Conference Series, 4008, eds. M. Iye, & A. F. Moorwood, 934

Chu, Y. Q., & Cui, X. Q. 1996, in Ground-Based Astronomy in Asia, Proceedings of the third East-Asian meeting on astronomy (Tokyo, Japan), ed. N. Kaifu, 327

Cui, X., Su, D., Li, G., et al. 2004, in Society of Photo-Optical Instrumentation Engineers (SPIE) Conference Series, 5489, ed. J. M. Oschmann, Jr., 974

Cui, X., Su, D.-Q., Wang, Y.-N., et al. 2010, in Society of Photo-Optical Instrumentation Engineers (SPIE) Conference Series, 7733, eds. L. M. Stepp, R. Gilmozzi, & H. J. Hall, 773309-8

Cui, X., & Yang, D. 1998, in Society of Photo-Optical Instrumentation Engineers (SPIE) Conference Series, 3352, ed. L. M. Stepp, 378

Gong, X., Cui, X., & Ye, X. 2004, in Society of Photo-Optical Instrumentation Engineers (SPIE) Conference Series, 5495, eds. J. Antebi, & D. Lemke, 499

Gunn, J. E., & Knapp, G. R. 1993, in Sky Surveys. Protostars to Protogalaxies, 43, ed. B. T. Soifer, 267

Hao, L. K., Jin, G., Wang, J., et al. 2005, Acta Astronomica Sinica, 46, 225

Hao, W. 2004, Experiment Research and Computation Analysis of LAMOST Dome (Ph.D. Thesis)

Hou, Y., Zhu, Y., Hu, Z., Wang, L., & Wang, J. 2010, in Society of Photo-Optical Instrumentation Engineers (SPIE) Conference Series, 7735, eds. I. S. McLean, S. K. Ramsay, & H. Takami, 77350C-9

Huo, Z.-Y., Liu, X.-W., Yuan, H.-B., et al. 2010, RAA (Research in Astronomy and Astrophysics), 10, 612

Jones, D. J. 1994, Appl. Opt., 33, 7362

Koleva, M., Prugniel, P., Bouchard, A., & Wu, Y. 2009, A&A, 501, 1269

Lasker, B. M., Lattanzi, M. G., McLean, B. J., et al. 2008, AJ, 136, 735

Lemaitre, G. 1984, in IAU Colloq. 78: Astronomy with Schmidt-Type Telescopes, Astrophysics and Space Science Library, 110, ed. M. Capaccioli, 533

Lemaitre, G. R. 2009, Astronomical Optics and Elasticity Theory: Active Optics Methods, Astronomy and Astrophysics Library, (Berlin: Springer)

Li, G., Gu, B., Yang, D., Wang, G., & Wang, Y. 2003, in Society of Photo-Optical Instrumentation Engineers (SPIE) Conference Series, 4837, eds. J. M. Oschmann, & L. M. Stepp, 284

Li, H.-N., Zhao, G., Christlieb, N., et al. 2010, RAA (Research in Astronomy and Astrophysics), 10, 753

Liu, G. R., & Yuan, X. Y. 2005, Acta Astronomica Sinica, 46, 331

Luo, A., & Zhao, Y. 2001, Nuovo Cimento B Serie, 116, 879

Luo, A.-L., Zhang, Y.-X., & Zhao, Y.-H. 2004, in Society of Photo-Optical Instrumentation Engineers (SPIE) Conference Series, 5496, eds. H. Lewis & G. Raffi, 756

Luo, A.-L., Wu, Y., Zhao, J., & Zhao, G. 2008, in Society of Photo-Optical Instrumentation Engineers (SPIE) Conference Series, 7019, eds. A. Bridger, & N. Radziwill, 701935-11

Luo, A., et al. 2012a, in preparation

Luo, A., et al. 2012b, RAA (Research in Astronomy and Astrophysics), 12, 1243

Mast, T. S., & Nelson, J. E. 1982, Appl. Opt., 21, 2631

Morales, I., Montero-Dorta, A. D., Azzaro, M., et al. 2012, MNRAS, 419, 1187

Newberg, H. J., Bai, Z., Beers, T., et al. 2012, in American Astronomical Society Meeting Abstracts, 219, #428.21

Noethe, L., Franza, F., Giordano, P., et al. 1988, Journal of Modern Optics, 35, 1427

Perryman, M. A. C., Lindegren, L., Kovalevsky, J., et al. 1997, A&A, 323, L49

Prugniel, P., & Soubiran, C. 2001, A&A, 369, 1048

Ren, J., Wang, J., Li, F. H., K., et al. 2007, Acta Astronomica Sinica, 48, 500

Saunders, W., Bridges, T., Gillingham, P., et al. 2004, in Society of Photo-Optical Instrumentation Engineers (SPIE) Conference Series, 5492, eds. A. F. M. Moorwood, & M. Iye, 389

Schmidt, B. 1931, Central-Zeitung für Optik und Mechanik, 52, 25

Smith, G. A., Saunders, W., Bridges, T., et al. 2004, in Society of Photo-Optical Instrumentation Engineers (SPIE) Conference Series, 5492, eds. A. F. M. Moorwood, & M. Iye, 410

Su, D. 1958, Journal of Teaching and Research of Nanjing University, Natural Science No.1

Su, D. 1962, Journal of Nanjing University (Astronomy), 25

Su, D. Q. 1988, Acta Astronomica Sinica, 29, 384

Su, D.-Q., Cao, C., & Liang, M. 1986, in Society of Photo-Optical Instrumentation Engineers (SPIE) Conference Series, 628, ed. L. D. Barr, 498

Su, D. Q., Cui, X., Wang, Y., & Yao, Z. 1998, in Society of Photo-Optical Instrumentation Engineers (SPIE) Conference Series, 3352, ed. L. M. Stepp, 76

Su, D.-Q., Jiang, S.-T., Zou, W.-Y., et al. 1994, in Society of Photo-Optical Instrumentation Engineers (SPIE) Conference Series, 2199, ed. L. M. Stepp, 609

Su, D.-q., Zou, W., Zhang, Z., et al. 2000, in Society of Photo-Optical Instrumentation Engineers (SPIE) Conference Series, 4003, ed. P. Dierickx, 417

Su, D.-Q., Jia, P., & Liu, G. 2012, MNRAS, 419, 3406

Su, D., & Cui, X. 1999, Progress in Astronomy, 17, 1

Su, D.-Q., & Cui, X.-Q. 2004, ChJAA (Chin. J. Astron. Astrophys.), 4, 1

Su, D., & Wang, Y. 1997a, Acta Astrophysica Sinica, 17, 202

Su, D., & Wang, Y. 1997b, Acta Astrophysica Sinica, 17, 315

Uomoto, A., Smee, S., Rockosi, C., et al. 1999, in American Astronomical Society Meeting Abstracts, Bulletin of the American Astronomical Society, 31, 1501

Wang, J., Jin, G., Huang, K., et al. 2005, Publications of the National Astronomical Observatories of China, 2, 114

Wang, L.-J., & Su, D.-Q. 1983, Acta Optica Sinica, 3, 132

Wang, S., & Su, D. 1992, in European Southern Observatory Conference and Workshop Proceedings, 42, ed. M.-H. Ulrich, 105

Wang, S.-G., Su, D.-Q., & Hu, Q.-Q. 1994, in Society of Photo-Optical Instrumentation Engineers (SPIE) Conference Series, 2199, ed. L. M. Stepp, 341

Wang, S.-G., Su, D.-Q., Chu, Y.-Q., Cui, X., & Wang, Y.-N. 1996, Appl. Opt., 35, 5155

Wei, M., & Stover, R. J. 1996, Solid State Sensor Arrays and CCD Cameras, San Jose, 226

Willstrop, R. V. 1984, MNRAS, 210, 597

Wilson, R. N., Franza, F., & Noethe, L. 1987, Journal of Modern Optics, 34, 485

Wilson, R. N., 2002, Reflecting Telescope Optics II (Springer Verlag)

Wu, X.-B., Chen, Z.-Y., Jia, Z.-D., et al. 2010a, RAA (Research in Astronomy and Astrophysics), 10, 737

Wu, X.-B., Jia, Z.-D., Chen, Z.-Y., et al. 2010b, RAA (Research in Astronomy and Astrophysics), 10, 745

Wu, Y., Luo, A.-L., Li, H.-N., et al. 2011a, RAA (Research in Astronomy and Astrophysics), 11, 924

Wu, Y., Singh, H. P., Prugniel, P., Gupta, R., & Koleva, M. 2011b, A&A, 525, A71

Wynne, C. G. 1989, MNRAS, 236, 47P

Xing, X., Zhai, C., Du, H., et al. 1998, in Society of Photo-Optical Instrumentation Engineers (SPIE) Conference Series, 3352, ed. L. M. Stepp, 839

Xu, W., Yu, Y., Zhang, M., Xu, Z., & Chen, J. 1997, Acta Astrophysica Sinica, 17, 135

Xue, Y., & Shi, H.-M. 2008, ChJAA (Chin. J. Astron. Astrophys.), 8, 580

Yang, D., Chen, K., Liang, Y., & Cui, X. 2005, in Society of Photo-Optical Instrumentation Engineers (SPIE) Conference Series, 5877, ed. A. E. Hatheway, 307

Yang, S. 1957, ACTA ASTRONOMICA SINICA, 5, 1

Yang, S., & Zhang, Z. 2008, in Society of Photo-Optical Instrumentation Engineers (SPIE) Conference Series, vol. 7019, eds. A. Bridger, & N. M. Radziwill, 70192B-8

Yao, Z. 1998, LAMOST internal technical report, 98-007

Yao, Z., Cui, X., Tan, D., & Zhang, Z. 2000, in Society of Photo-Optical Instrumentation Engineers (SPIE) Conference Series, 4004, eds. T. A. Sebring, & T. Andersen, 164

Yao, Z. q., Hao, W., Zhou, F., Shi, H., & Chen, Z. 2003, in Society of Photo-Optical Instrumentation Engineers (SPIE) Conference Series, 4837, ed. J. M. Oschmann, & L. M. Stepp, 198

Yao, S., Liu, C., Zhang, H.-T., et al. 2012, RAA (Research in Astronomy and Astrophysics), 12, 772

Yi, Z. P., Luo, A., Zhao, Y. H., et al. 2012, in preparation (M catalog release)

Yuan, H.-B., Liu, X.-W., Huo, Z.-Y., et al. 2010, RAA (Research in Astronomy and Astrophysics), 10, 599

Yuan, H., et al. 2012, Proc. SPIE, 8448-88

Zhang, Y. 2008, in Society of Photo-Optical Instrumentation Engineers (SPIE) Conference Series, 7012, ed. L. M. Stepp, & R. Gilmozzi, 70123H-11

Zhang, Y., & Cui, X.-Q. 2005, ChJAA (Chin. J. Astron. Astrophys.), 5, 302

Zhao, G., Zhao, Y.-H., Chu, Y.-Q., Jing, Y.-P., & Deng, L.-C. 2012, RAA (Research in Astronomy and Astrophysics), 12, 723

Zhao, Y. 1999, in Observational Astrophysics in Asia and its Future, 4th East Asian Meeting on Astronomy (4th EAMA), ed. P. S. Chen, 1

Zhu, Y., Hu, Z., Zhang, Q., Wang, L., & Wang, J. 2006, in Society of Photo-Optical Instrumentation Engineers (SPIE) Conference Series, 6269, eds. I. S. McLean, & M. Iye, 62690M

Zhu, Y., Hu, Z.W., Wang, L., et al. 2011, Sci Sin-Phys Mech Astron, 41(11), 1337

Zou, S., & Wang, G. 2006, in Society of Photo-Optical Instrumentation Engineers (SPIE) Conference Series, 6269, eds. I. S. McLean, & M. Iye, 626922

Zou, H., Yang, Y.-B., Zhang, T.-M., et al. 2011, RAA (Research in Astronomy and Astrophysics), 11, 1093